The Photophysics of Ruddlesden-Popper Perovskites: A Tale of Energy, Charges and Spins

Marcello Righetto[†,1,2], *David Giovanni*[†,1], *Swee Sien Lim*[1], *Tze Chien Sum*[1,*]

[1]Division of Physics and Applied Physics, School of Physical and Mathematical Sciences, Nanyang Technological University, 21 Nanyang Link, Singapore 637371, Singapore

[2]Department of Physics and Astronomy and London Centre for Nanotechnology, University College London, London WC1E 6BT, United Kingdom.

Email: Tzechien@ntu.edu.sg

[†]Authors contributed equally

Abstract

Quasi two-dimensional halide perovskites (also known as Ruddlesden-Popper or RPs) are the most recent and exciting evolution in the perovskite field. Possessing a unique combination of enhanced moisture and material stability, whilst retaining the excellent optoelectronic properties, RPs are poised to be a game changer in the perovskite field. Spurred by their recent achievements in solar cells, light-emitting diodes and spintronic devices, these materials have garnered a mounting interest. Herein, we critically review the photophysics of RPs and distil the science behind their structure-property relations. We first focus on their structure and morphology by highlighting the crucial role of large cations: dictating the RPs' layered structure and the statistical distribution of thicknesses (*i.e.*, *n*-phases). Next, we discuss how optoelectronic properties of RPs differ from conventional halide perovskites. Structural disorder, stronger excitonic and polaronic interaction shape the nature of photo-excitations and their fate. For example, faster recombinations and hindered transport are expected for charge carriers in thinner *n*-phases. However, the complex energetic landscape of RPs, which originates from the coexistence of different n-phases, allows for funnelling of energy and charges. Presently, the photophysics of RPs is still nascent, with many recent exciting discoveries from coherence effects in the above-mentioned funnelling cascade to spin effects. Giant Rashba spin-orbit coupling, also observed in RPs, dictates their spin dynamics and provides exciting spintronics opportunities. To leverage these propitious RPs, future research must entail a cross-disciplinary approach. While materials engineering will unlock new chiral RPs and Dion-Jacobson variants, novel characterization techniques such as in situ synchrotron-based X-ray diffraction, ultrafast electron microscopy, and multi-dimensional electronic spectroscopy *etc.* are essential in unravelling their secrets and unleashing their full potential.

1. Introduction

In the past decade, halide perovskites (HPs) have taken the optoelectronics research community by storm. HPs based solar cell has reached the record efficiency of 25.2%, thus overcoming efficiencies that could only be achieved after four decades of intensive research and development on silicon photovoltaics [1]. The unique combination of facile, low-cost manufacturing and high efficiencies motivates an unwavering interest in these materials [2]. This tremendous interest has led to the exploration of higher-hanging fruits of HPs, such as light-emitting devices [3], hot carrier physics [4, 5], quantum technologies [6], photocatalysis and many other applications beyond photovoltaics [7].

Conventional HPs are described by the stoichiometric formula ABX_3, where A is a monovalent cation (*e.g.*, Cs^+, $CH_3NH_3^+$, $NH_2CHNH_2^+$, etc.); B is a divalent metal ion (*e.g.*, Pb^{2+}, Sn^{2+}, etc.); and X is halide anion (*e.g.*, Cl^-, Br^-, I^-) [8]. In this crystalline structure, A cation's dimension is required to meet stringent requirements, empirically determined by the Goldschmidt's tolerance factor, to allow the formation of a perovskitic inorganic network [9]. To the first approximation, the A cation primarily plays a geometrical role, not directly participating in the band-edge electronic structure but instead templating the assembly of B and X ions and dictating dimensions of this network [8]. However, more complex phenomena related to the A cations have been demonstrated [10, 11]. $[BX_6]^{4-}$ octahedra are building blocks of a three-dimensional corner-sharing network that confers HPs with a high structural and electronic dimensionality, thus laying the foundations of their success in optoelectronic applications [12, 13]. Indeed, the startling achievements of HPs in photovoltaics stem from an ideal combination of a direct bandgap system with suitable energy, high absorption cross-section extending to the near-infrared region, a long-range balanced carrier diffusion, a defect tolerant electronic structure, and a small exciton binding energy [14-18].

Many of these photophysical properties paved the way for further development of HPs in light-emitting devices (PeLEDs), thereby confirming once again the complementarity between a great solar cell and a great light-emitting device [19]. Building upon the vast knowledge developed for photovoltaics, PeLED external quantum efficiencies (EQEs) have surged from 0.76% to above 20% in five years. However, recent successes of PeLEDs coincided with the development of lower-dimensional perovskites phases, among which the so-called Ruddlesden-Popper phases (RPs), currently at the nexus of optoelectronic research.

In RPs, the geometrical and templating role of the A cation is taken to the extreme, with the introduction of another additional large cation (LC) that cannot fit the cavities of the HP inorganic network. Its templating effect results in the disruption of the perovskite lattice to form multiple inorganic HP sheets, separated by LC in a layered structure with stacking direction perpendicular to the (100) plane [20-22]. Although other families (*e.g.*, (110)- and (111)- oriented) of lower-dimensional lead halide perovskite were synthesized, this review will focus on the (100)-oriented family, while the interested reader is referred to more comprehensive reviews by Mitzi and Kanatzidis [23, 24].

From a technological point of view, RPs are good candidates to overcome stability issues that are plaguing HPs for two main reasons: (i) the hydrophobic character of LCs provides more efficient isolation of the ABX_3 sub-lattice from the moisture [22, 25]; and (ii) the higher formation enthalpies make this lattice more resistant towards its decomposition [26, 27]. However, this additional complexity introduces new disorder and instabilities, such as the disproportion of thicker RP phases, which results in a spontaneous assembly of mixed thickness phases, often referred to as a multiple quantum well (MQW) system [28]. Hence, the choice of

LCs and the stoichiometry are significant additional degrees of freedom that can help to tune the properties of RPs. Similarly, the photophysics of these systems is radically changed. Indeed, the introduction of LCs disrupts the electronic dimensionality (*i.e.*, the connectivity of the octahedra $[BX_6]^{4-}$). This disruption has a silver lining: modifications of the bandgap and increased exciton binding energies are crucial factors in the current applications of RPs. Furthermore, the increased number of surfaces and the introduction of LC increase their softness and re-determine their carrier-phonon coupling.

Hence, a deep understanding of the complex photophysics underlying RP is critical not only to explicate their recent successes in devices, such as PeLEDs, but also to envision and steer their innovative application. In this review, we describe the photophysics of RP, focusing firstly on the structural variety in RP and defining the structure-photophysics property relations. The second part will focus on the nature of the carriers and their recombination dynamics. Finally, we describe various types of funneling processes (*e.g.,* energy, charge, and spin) within mixed RP systems, with particular attention to new opportunities and prospects.

2. Structure and structure-properties relationship

2.1. Crystal Structure

In three-dimensional HPs, the cation choice is strictly subordinate to geometrical considerations, usually summarized by the Goldschmidt tolerance factor (t) [9, 24]. The stability range for lead HP is indicatively between 0.8 and 1 [29], limiting the choice of the A cation to three cations (MA, FA, Cs). Conversely, in RPs, the layered structure relaxes this constraint and allows accommodating bulkier cations, opening to a virtually unlimited library of large cations (LCs) [23].

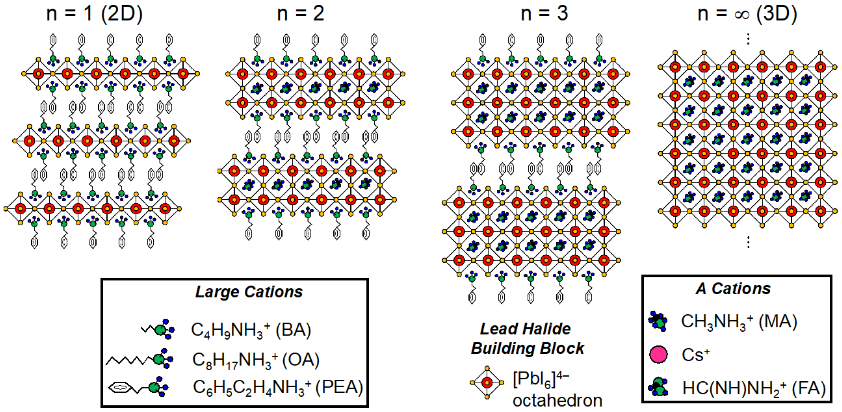

Figure 1. Schematic description of (100)-oriented family of RP. Conventional R-NH_3^+ large cations and A cations are described in the insets. The schematic shows a possible example of phenyl-ethyl ammonium large cation. With increasing *n*, the thickness on the inorganic layer increases. This family ranges from 2D phenyl-ethyl ammonium lead iodide (PEPI) to 3D methylammonium lead iodide (MAPI) perovskite.

As shown in **Figure 1**, by observing the crystallographic direction <100>, the resulting structure is layered: layers of HP are stacked between layers of large organic cations. The resulting stoichiometric formula $LC_2A_{n-1}B_nX_{3n+1}$ defines n as the number of HP layers sandwiched between the LC, part of a supercell that is repeated in the RP crystal structure. The LCs act as spacers between different HP layers, which are held together by a combination of Coulombic forces, strong Van der Waals interactions, and hydrophobic interactions. Hence, RPs can be described as a class of superlattice semiconductors, reminiscent of the complex inorganic MQW (*e.g.*, AlGaAs/GaAs heterostructures).

Although the choice of the LC is virtually unlimited, because of the relaxed geometrical constraint, some guidelines were established in the pioneering work of Mitzi [21, 30-32].

Ammonium ions are usually preferred because of their ability to interact ionically and form hydrogen bonds with the anionic MX^{6-} framework. These interactions drive the assembly, orientation, and conformation of the organic moieties in the LC layer. In this scheme, the steric interaction that is controlled by the footprint of the inorganic framework determines the main geometrical constraints. As estimated by Mitzi for lead iodide structures, the cross-sectional area available is around 40 $Å^2$, and therefore can accommodate a variety of different organic cations [30]. Yet other essential considerations stem from the degree of octahedral distortion induced by these different cations. Indeed, the competition between stereochemical demands of the two cations (*i.e.*, A and LC) forces the surface octahedra to rotate and induces a Pb-I-Pb angle different from the 163.55° of bulk $MAPbI_3$, for instance [20, 24]. This rotation is a further degree of freedom that can be controlled with the thickness and the choice of the cation, opening to white light emitters, discussed further in **Section 4.3**. For a complete library of LC used insofar in RPs, the reader is referred to the excellent Perspective by Kanatzidis [23]. It is worth noting that two-dimensional layered RPs structures can be obtained by introducing not only LCs but also large anions, such as in the case of pseudo-halides, *e.g.*, $MA_2Pb(SCN)_2I_2$.[33] Despite early calculations suggesting these materials as promising candidates for single junction solar cells ($E_g < 1.5$ eV), more recent studies reveal that their structure and properties resemble those of other two-dimensional RPs.[34]

Owing to a relatively well-understood and straightforward structure, most of the photophysics studies focus on RPs based on aromatic and aliphatic primary ammonium LCs ($R\text{-}NH_3^+$), such as phenyl-ethyl and butyl- ammonium (PEA and BA, respectively). These phases ($PEA_2MA_{n-1}Pb_nI_{3n+1}$ and $BA_2MA_{n-1}Pb_nI_{3n+1}$) were introduced almost 30 years ago, by the pioneering work of Calabrese and Ishihara, and constitute an ideal platform for photophysics studies [35, 36].

Therefore, this review will focus mostly on their properties. Yet the introduction of other moieties and more complicated R- cations that can interact among themselves is a field still in its infancy. Hence, pioneering works and areas of possible development will be highlighted throughout the paper.

2.2. Thin Film Morphology

The thermodynamical stability of lead iodide RPs decreases with the increasing n index. As demonstrated by Kanatzidis *et al.*, high n-phases ($n > 5$) have a positive enthalpy of formation, higher than the bulk HPs one [27]. The thermodynamical instability of high-n RP phases epitomizes how the synthesis of RPs requires an accurate control on both thermodynamic and kinetic aspects. Whilst isolation and synthesis of pure n-phase RPs provided an essential platform to delve deeper into the physics of these systems, many groups reported advancements based on RP thin films containing a distribution of n-phases (henceforth mixed RPs). The synthesis protocol for the formation of mixed RPs films follows closely that for the synthesis of bulk MAPI: spin coating of the precursors salt dissolved in DMF/DMSO/γ-butyrolactone and mixtures thereof, usually completed with antisolvent dripping and annealing steps. Despite an overall stoichiometry being imparted by choice of relative ratios between the precursor salts, mixed RPs thin films often contain a statistical distribution of n-phases, in the absence of precise phase control strategies [22, 35, 37]. Quintero-Bermudez *et al.* recently demonstrated that a log-normal distribution peaked at $\langle n \rangle$ (*i.e.*, the stoichiometric n value) when a homogeneous LC is present in the thin film, although differences in relative LC solubilities could lead to shifts [38]. Kanatzidis's group pioneered the synthesis of phase pure RP thin films and demonstrated the use of single-crystal precursors as a viable approach to control the phase-purity [28, 39-41].

Controlling the relative orientation of *n*-phases in both pure and mixed RPs thin films is another crucial challenge; holding promises to boost performances of RP-based devices. This has been demonstrated clearly with the introduction of the so-called hot-casting technique. Besides controlling the phase distribution, the relative orientation is also influenced [38, 39, 42]. Thin films synthesized with these procedures create a concentration gradient of *n*-phases with a higher concentration of low *n*-phases at the top of the film. This gradient has been exploited by many groups to impart directionality in carrier transport [43, 44].

The relative orientation of the phases, and the degree of order in mixed RPs thin films, are generally determined by grazing incidence small and wide-angle x-ray scattering, *i.e.*, GISAXS and GIWAXS techniques, as shown in **Figure 2a-d**. Using these techniques, Quintero-Bermudez *et al.* [38] reported that, for homogeneous nucleation, the relative orientation depends on the $\langle n \rangle$ value, with lower *n*-phases distributing preferentially aligned with the substrate, while high *n*-phases aligning in the perpendicular direction, as shown in **Figure 2**. Also, the difference between GIWAXS patterns in **Figure 2a-d** makes it evident how hot casting can be used to impart order to these mixed films.

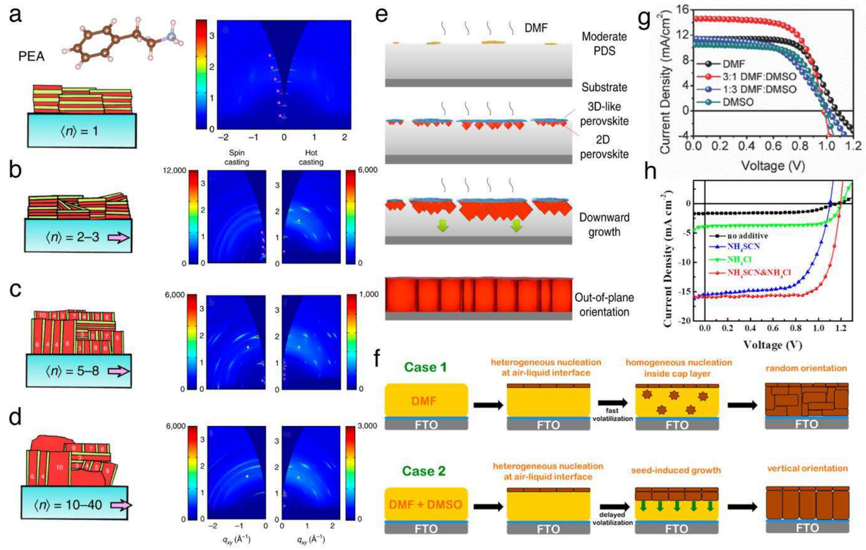

Figure 2. (a-d) Analysis of relative orientations in mixed RPs films of $PEA_2MA_{n-1}Pb_nI_{3n+1}$ with increasing average ⟨n⟩, and comparison between spin casting and hot casting deposition techniques. While PEPI (*i.e.*, ⟨n⟩ = 1) presents a perfect in-plane alignment (pink dots), with increasing ⟨n⟩ more out-of-plane aligned phases are present. Figure (a-d) are reproduced with permission from Nat. Mater. **17**, 900 (2018). Copyright 2018 Springer Nature [38]. (e) Illustration of nucleation and growth mechanisms for vertically aligned mixed RPs with the use of NH_4Cl additive excess. The reduced quantity of PbI_2-solvent solvated (PDS) phases induces the heterogeneous nucleation of RPs at the air-liquid interface and templates the growth. Wang et al. Nat. Commun. **11**, 582 (2020); licensed under a Creative Commons Attribution (CC BY) license [45]. (**f**) Analogous heterogeneous nucleation mechanism obtained by solvent engineering. Reproduced with permission from ACS Sustainable Chem. Eng. **7**, 3487 (2019). Copyright 2019 American Chemical Society [46]. Comparison between photovoltaic performances of solvent engineered $(BA)_2(MA)_4Pb_5I_{16}$ (**g**) and additive engineered (**h**) $(PEA)_2(MA)_4Pb_5I_{16}$ RPs thin films. Figure (g) is reproduced with permission from Adv. Energy Mater. **8**(1) 1700979 (2018), Copyright 2018 Wiley and Sons [41]. Figure (h) is reproduced with permission from ACS Energy Lett. **3**(9) 2086 (2018). Copyright 2018 American Chemical Society [47].

This quest for exerting control in mixed RPs thin films resulted in many possible synthetic strategies developed in the past few years. Possible ways of controlling the orientation include careful procedures for solvent engineering, temperature tuning, and additives [41, 45-52]. Choi's group demonstrated how vertically-oriented $BA_2MA_3Pb_4I_{13}$ can be grown exploiting the heterogeneous nucleation of RP phases at the air-solvent interface [53, 54]. As shown in **Figure 2e** and **f**, the use of additives and the fine-tuning of solvents and temperature aims to favor this heterogeneous nucleation. Resulting vertically aligned thin films demonstrated better photovoltaic performances with respect to randomly oriented, as shown in **Figure 2g-h**. For a more detailed overview of the possible strategies, the interested reader is referred to the nice review by K. Zhu *et al.* [55]. These strategies could prove to be of utmost importance for the LED field. Recently, many groups have also harnessed the statistical distribution of mixed RP phases to realize highly efficient LEDs based on excitation funneling and inherently charge separating heterostructures [56-58] and the perspective of funneling in ordered and oriented mixed RPs thin film holds much potential in this field. Many of these concepts will be analyzed in detail in **Section 4.5**.

3. Electronic Band Structure: Quantum and dielectric confinement

3.1. Band structure

The electronic band structure of $(LC)_2(MA)_{n-1}Pb_nI_{3n+1}$ RPs is based on that of $MAPbI_3$. The $MAPbI_3$ band structure has been heavily studied in the past decade, and the interested reader is referred to many comprehensive reports on this matter [59, 60]. Briefly, the optical transitions in $MAPbI_3$ above the bandgap lead to the promotion of electrons from Pb(6s)-I(5p) (*s*-like) to Pb(6p) (*p*-like) states in the valence and conduction bands, respectively (**Figure 3a**) [8, 61, 62]. However, in RPs, the reduced electronic dimensionality (*i.e.*, the connectivity of the $[PbI_6]^{4-}$ octahedra) and the layered structure introduce both quantum and dielectric confinement effects in the inorganic layers. Quantum confinement effects arise from 2D constricted motion of the carriers, where the composite material can be described as a Type-I heterostructure [30, 63]. Yan and co-workers reported DFT calculation for $Cs_{n+1}Pb_nI_{3n+1}$, where the role of quantum confinement emerged from the analysis of band-structures and increased bandgap was observed for lower *n* phases (**Figure 3b**), as a result of the reduced electronic dimensionality. Furthermore, Nurmikko *et al.* first introduced the concept of RP as "dielectric quantum wells" (**Figure 3c**), where the lower dielectric constant of the barrier further enhances carrier confinement [64, 65]. Recently, these two types of confinement were combined in a first principle model by Even *et al*. that confirmed how the carriers are confined in the sub-nanometre perovskite layer [63, 66-68]. Both early and more recent studies were able to reproduce the bandgap increase with decreasing of the well thickness (*i.e.*, the *n* value), as reported in **Figure 3d** [61, 69]. For a more detailed description, we refer the reader to the comprehensive review by Even, Katan *et al.* [66, 67].

A closer look at the band structures in **Figure 3b** reveals how confinement affects not only the band gap but also effective masses of the carriers (*i.e.*, the curvature of conduction band minima and valence band maxima). As quantified by Yan and co-workers [12], the hole and electron effective masses, m_h^* and m_e^*, are higher in the direction perpendicular to the layers, as a consequence of disrupted electronic dimensionality. Interestingly, confinement affects them even in the in-plane direction: here, m_h^* and m_e^* increase with decreasing *n* number. Increased effective mass values are expected to both hinder transport properties and enhance the excitonic character of thinner RPs, as discussed in the next Section.

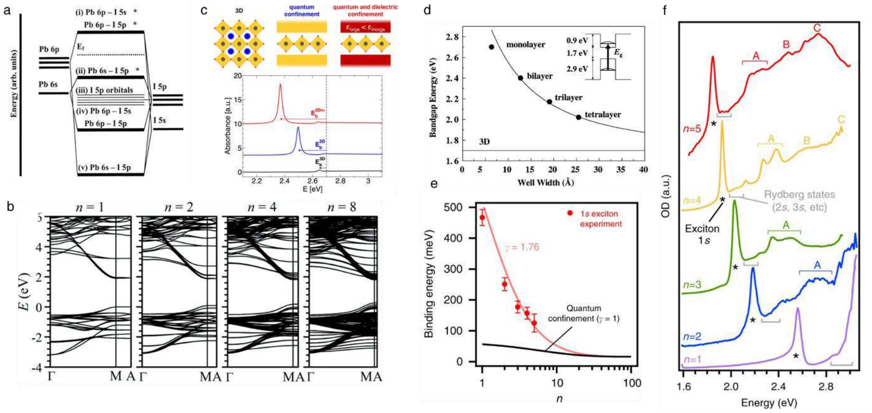

Figure 3 (a) Linear combination of atomic orbital diagram for the Pb-I bonds in $[PbI_4]^{6-}$, representative of the band structure for lead halide perovskites. Reproduced with permission from Phys. Rev. B **67**(15), 155405 (2003). Copyright 2003 American Physical Society [62]. (b) DFT calculation of $Cs_{n+1}Pb_nI_{3n+1}$ electronic band structure for different n phases. Reproduced with permission from Mater. Horiz. **4**, 206 (2017). Copyright 2017 Royal Society of Chemistry [12]. (c) Computed deconvolution of quantum confinement (blue line) and quantum confinement corrected with dielectric confinement, for a slab of $(Decyl\text{-}NH_3)_2PbI_4$. Reproduced with permission from ACS Nano **10**(11), 9776 (2016). Copyright 2016, American Chemical Society [68]. (d) Optical bandgap energy of $(C_6H_{13}NH_3)_2(MA)_{n-1}Pb_nI_{3n+1}$ as a function of the well thickness. Experimental data (black points) well match energies calculated with effective-mass approximation, using energies in the inset. Reproduced with permission from Sci. Technol. Adv. Mater. **4**(6), 599 (2003). Copyright 2003 Elsevier Science [61]. (e) Exciton binding energy scaling law against the n-phase number for $(BA)_2(MA)_{n-1}Pb_nI_{3n+1}$ RP. The red curve represents a general scaling law of the EBE, the comparison with the scaling law for quantum confined systems reveal the role of dielectric confinement. Blancon et al. Nat. Commun. **9**(1), 2254 (2018); licensed under a Creative Commons Attribution (CC BY) license [70]. (f) Optical absorption spectroscopy for $(BA)_2(MA)_{n-1}Pb_nI_{3n+1}$ RP single crystals with increasing *n*. Blancon et al. Nat. Commun. **9**(1), 2254 (2018); licensed under a Creative Commons Attribution (CC BY) license [70].

3.2. *Exciton Binding Energy*

As suggested by changes in the band structure and in the dielectric landscape, confinement dramatically enhances the stability of photogenerated excitons, quantified in terms of large exciton binding energies (EBE). Enhanced EBEs shown in **Figure 3e** are reflected in the evolution of the absorption lineshapes, which evolve from step-like functions in bulk lead halide perovskite to well-resolved Lorentian lineshapes for *n* = 1 RP perovskites [71] (**Figure 3f**). The strongly excitonic nature of *n*=1 systems was confirmed in the early experimental studies of the 1990s [35, 36]. The comparison between $(C_{10}H_{21}NH_3)_2PbI_4$ (where the dielectric constant of the spacer is $\epsilon_s = 2.44$) and $(PEA)_2PbI_4$ (with a higher $\epsilon_s = 3.32$) revealed a strong dependency of the EBE on the ϵ_s value, with reported EBE values of about 320 and 220 meV, respectively [64, 65]. In this context, exfoliation was reported to play a significant role: up to 490 meV EBE were reported for exfoliated $(BA)_2PbI_4$, while their single crystal counterpart was reported to have EBE of 370 meV [72].

Higher *n* phases were introduced for tin-based perovskites by Mitzi *et al.* in 1994 [73] and the optical properties of lead iodide-based high-*n* RPs were first reported in 1995 [74]. Kondo *et al.* reported a comprehensive study on the optical properties of mixed *n* phases of *n* = 2 and 3 [61]. More recently, higher accuracy in determining their bandgap and EBE was achieved, thanks to the advancements in the synthesis of phase pure high *n* RPs [28, 40]. Reported bandgap for phase pure $(BA)_2(MA)_{n-1}Pb_nI_{3n+1}$ evolves from 2.17 eV (*n* = 2) to 1.85 eV (*n* = 5). Blancon *et al.* reported 380 meV, 270 meV, and an average of 220 meV for *n* = 1, *n* = 2 and *n* = 3-5, respectively [75]. More recently, Blancon *et al.* determined these values with low temperatures (4 K) measurements, and values of 471, 251, 177, 157, and 129 meV were reported for *n* = 1 to 5, respectively. Moreover, using magneto-optical measurements, the same study provided an accurate determination of the exciton reduced masses [70]. These advancements are summarized in a scaling law for EBE in RPs, based on the common definition for quantum confined systems:

$$E_b = \frac{E_0}{\left(1 + \frac{\alpha - 3}{2}\right)^2}, \tag{1}$$

with,

$$\alpha = 3 - \gamma e^{-\frac{L_w}{2a_0}}. \tag{2}$$

Here, E_0 and a_0 being the values for bulk $MAPbI_3$ (16 meV, and 4.1 nm, respectively). As shown in **Figure 3e**, RPs deviate from the expected value for 2D confinement ($\gamma = 1$) and are well described by $\gamma = 1.76$ for $(BA)_2(MA)_{n-1}Pb_nI_{3n+1}$ [70]. These deviations not only further confirm the great role played by the dielectric confinements but also suggest possible variations of the exciton Bohr radius for different *n* values.

4. Nature of photoexcitation and their dynamics

4.1. Initial photoexcitation

All the optical dynamics of the excited states begin with the photon absorption process. For traditional direct-bandgap semiconductors, the initial photoexcitation originated from a linear absorption process can result in 3 different photoexcited species: [76, 77]: (i) non-resonant excitation of the free carriers (hot or “cold”), (ii) phonon-assisted non-resonant excitation of hot excitons, and (iii) resonant excitation of free exciton at the light cone and exciton dispersion intersection – **Figure 4**. Hot/cold here refers to additional excess energies that these photoexcited species have with respect to the thermal equilibrium with the lattice. The nature of the species is primarily determined by the incoming photon excess energy with respect to the materials’ bandgap and exciton resonances.

PLEASE CITE THIS ARTICLE AS DOI: 10.1063/5.0031821

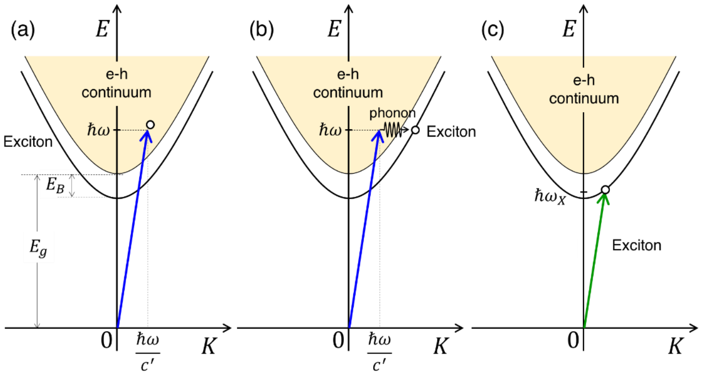

Figure 4. Linear photoexcitation nature of a direct bandgap semiconductor represented in a two-particle picture. Non-resonant photon energy will result in (a) free-carrier photoexcitation, or (b) phonon-assisted hot-exciton photoexcitation. Meanwhile, (c) resonant photon energy will result in direct photoexcitation of free excitons. Here, the K represents the total momentum of electron and hole.

During the thermalization process, following the initial photoexcitation, in these carriers with excess energy will first thermalize via carrier-carrier scattering process (between 10-85 fs for 3D perovskite [78]) to form a Fermi-Dirac distribution for carriers, (or Bose-Einstein distribution for exciton), which can be described by a temperature. Assuming initial excitation of hot carriers (**Figure 4a**), which is the most common case, such thermalization will cool down into thermal equilibrium with the lattice, by emitting LO phonons. Once the kinetic energy of the carriers is low enough, they could form excitons. Some studies have suggested that such hot-carriers cooling process can be tuned in RP perovskites by varying the dielectric properties of the LCs, due to the screening of Fröhlich interaction [79, 80]. However, this subject requires further study to achieve a complete understanding and utilizing these hot carriers in RP perovskites.

4.2. Excitons or Free carriers?

In contrast to their initial nature immediately after the photoexcitation, the possible thermally equilibrated nature of the photoexcited species are more complex. One of the most recurring open questions appearing in the literature, especially in the context of halide perovskites [77, 81-84], is whether the photoexcited species is dominated by excitons or free carriers. Again, from the literature, one of the most prevalent methods used to determine the ratio between these two species is the Saha equation [77, 82-84]. This equation describes the exciton formation and dissociation in terms of a chemical equilibrium $X \Leftrightarrow e^- + h^+$. For *d*-dimension semiconductor (d = 2, 3), the fraction of free carrier to the total photoexcitation (*i.e.*, branching ratio $\alpha = n_\mathrm{f} / n_\mathrm{tot}$, with $n_\mathrm{tot} = n_\mathrm{f} + n_\mathrm{x}$; where n_x and n_f is the exciton and free carrier population respectively) is given by:

$$\frac{\alpha^2}{1-\alpha} = \frac{1}{n_\mathrm{tot}\lambda_\mathrm{T}^d} \exp\left(\frac{-E_\mathrm{b}}{k_\mathrm{B}T}\right) \tag{3}$$

Where $\lambda_T = h/\sqrt{2\pi\mu k_B T}$ is the De Broglie wavelength of the exciton; and $\mu = m_e m_h/(m_e + m_h)$ is the exciton reduced mass. There are several assumptions underlying this equation: (i) thermal equilibrium is reached before any recombination; and (ii) there is no screening effect, *i.e.*, constant EBE with respect to the photoexcited population. **Figure 5a-b** shows the plot of α as a function of n_tot for 3D and 2D semiconductors at 300 K.

Using this equation, D'Innocenzo *et al.* [82] inferred that at carrier concentration relevant for both typical device applications (n_tot ~ 10^{15} cm^{-3}) and optical experiments (n_tot ~ 10^{17} cm^{-3} for 3D, or n_tot ~ 10^{10} cm^{-2} for 2D), free carriers are dominant in bulk lead halide perovskites at room temperature (E_b < 100 meV). However, experimentally observed behavior goes beyond simple predictions from the Saha equation. In archetypal 3D $CH_3NH_3PbI_3$ ($E_\mathrm{b} \leq 15$ meV) and $CH_3NH_3PbI_xBr_{3-x}$ (E_b ~ 100 meV) perovskites, using transient absorption spectroscopy Sheng *et al.* [81] demonstrated exciton population of ~9% for the former; and while it is dominant for the latter, irrespective of pump intensities. Such an exciton-to-carrier branching ratio reported is much higher than predicted by the Saha equation (*i.e.*, expected to be ~0.1% and ~4% of free carriers at E_b = 10 meV and 100 meV, respectively, at n_{tot} = 10^{17} cm^2). From time-resolved PL analysis, Sarritzu *et al.* [77] observed a complicated transition from monomolecular, to bimolecular, back to monomolecular transition in $CH_3NH_3PbBr_3$ perovskite, with increasing excitation density. In view of the Saha equation, they concluded that the free carriers are still the main species, with the complex behavior arising from the interplay of higher exciton emission efficiency and non-radiative recombination channels.

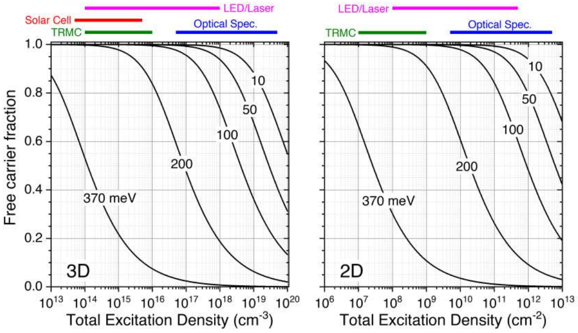

Figure 5. Plot of Saha equation for 3D and 2D semiconductors, with different exciton binding energies (in the unit of meV), at room temperature (300 K). The exciton reduced mass is set to be $0.1m_0$ (typical for perovskites), where m_0 is a free electron mass. The ranges of excitation density for several applications are illustrated.

This point is crucial for RP perovskites, where the EBE could go above 300 meV, (see **Section 3.2**). From the Saha equation, at n_{tot} = 10^{10} cm^{-2} (typical concentration of pulsed optical experiments on 2D perovskites, per quantum well), free carrier population counterintuitively is still dominant (~60%) even with binding energy as high as 200 meV – **Figure 5b**. Converse to this prediction, Xing *et al.* [85] and Marongiu *et al.* [71] showed how excitons are the dominant photoexcited species in lead-iodide based RPs. In a similar tone, Gelvez-Rueda *et al.*

[84], who by using time-resolved microwave conductivity (TRMC) measurement, determined free carrier branching ratio in $(BA)_2(MA)_{n-1}Pb_nI_{3n+1}$ mixed RPs with $\langle n \rangle$ = 1, 2, 3, and 4 RP, to be 5%, 50%, 85% and 95%, respectively (at room temperature and n_{tot} ~ 10^{15} cm^{-3} or ~ 10^{8} cm^{-2} per quantum well). Given the indicative values for estimated binding energies (370 meV, 170 meV, 120 meV, and 80 meV, respectively [84]), although the measured branching ratio follows the temperature-dependent trend predicted by the Saha equation, the measured free carrier populations are way below a simple estimation by the Saha equation (α ~ 25% for E_b =370 meV, and α > 99% for $E_b \leq 200$ meV).

In fact, opposite behavior between exciton and free-carrier trend as a function of total excitation has been reported by Cingolani *et al.* [86] in II-IV semiconductor quantum well systems. In typical Saha equation analysis where the EBE is fixed, at a given temperature, typically free carriers dominate at low n_{tot}, while it becomes increasingly excitonic with increasing n_{tot}. However, when the effect of bandgap renormalizations and screenings as a function of excitation densities are fully incorporated, Cingolani *et al.* demonstrated an inverse transition trend from exciton to free-carrier with increasing n_{tot}, [86]. Similar results were also reported in theoretical studies by Sekiguchi *et al.* [87], where density-dependent EBE could flip the typical Saha trend.

The deviation of experimental results of branching ratio values in RPs implies that it is not as simple as a prediction from the Saha equation. Thus, the problem remains: *How can we determine the branching ratio between exciton and free-carriers in RP perovskites?* This issue is still an open question, which requires further attention from both the experimental and theoretical viewpoints.

4.3. Polaron and self-trapping in RP perovskites

When a carrier or exciton exists in a deformable lattice, it creates an attractive potential well, in which it is momentarily trapped. Such potential originates mainly from the electron-phonon (e-ph) coupling, either long-range (optical phonons) or short-range (acoustic phonons) [88]. The former is usually described in terms of Fröhlich Hamiltonian and would create a so-called "large polaron", and whose radius spanning several to tens of lattice constant. A large polaron formation (weak coupling) typically results in the increase of the effective carrier mass $m^* \approx m_0^*(1+\alpha/6)$ for 3D, and $m^* \approx m_0^*(1+\pi\alpha/8)$ for 2D (where α is the Fröhlich polaron coupling constant, and m_0^* is the single-particle effective mass), while retaining its delocalization properties (free). The latter is usually described in terms of a deformation potential and would create a so-called "small-polaron" or "self-trapped" carriers/excitons, whose radius is within a single lattice constant and results in the localization.

The general case, where both long- and short-range interactions are present, can be described by the Toyozawa continuum model. For an electron with wavefunction $\psi(\boldsymbol{r})$, elastic dilation $\Delta(\boldsymbol{r})$, and electrostatic potential $\phi(\boldsymbol{r})$, the adiabatic energy could be described by a functional $E[\psi,\Delta,\phi]$ [88, 89]:

$$\begin{aligned} E[\psi,\Delta,\phi] = {} & \frac{\hbar^2}{2m}\int(\nabla\psi)^2\,\mathrm{d}\boldsymbol{r} + E_\mathrm{d}\int|\psi|^2\Delta\,\mathrm{d}\boldsymbol{r} + e\int|\psi|^2\phi\,\mathrm{d}\boldsymbol{r} + \frac{C}{2}\int\Delta^2\,\mathrm{d}\boldsymbol{r} \\ & + \frac{\epsilon_\mathrm{s}\epsilon_\infty}{8\pi(\epsilon_\mathrm{s}-\epsilon_\infty)}\int|\nabla\phi|^2\mathrm{d}\boldsymbol{r}. \end{aligned} \tag{4}$$

Where the right-hand side terms represent the kinetic energy, acoustic phonon interaction, electron-LO phonon coupling, elastic potential energy, and dielectric potential energy, respectively. The symbol E_d represents the deformation potential; C represents the elastic constant; ϵ_s and ϵ_∞ represent the static and high-frequency dielectric constants, respectively. Assuming a Gaussian wavepacket with radial extent a, and minimizing the functional sequentially in order of Δ and ϕ, the energy functional could be expressed in the terms of localization parameter λ as:

$$E(\lambda) = B[\lambda^2 - g_s\lambda^3 - g_l\lambda] \qquad \text{for 3D,} \qquad (5)$$

$$E(\lambda) = B[\lambda^2 - g_s\lambda^2 - g_l\lambda] \qquad \text{for 2D.} \qquad (6)$$

Here, the $\lambda \equiv a_0/a$, where a_0 is the lattice constant, with limits between 0 (delocalization) and 1 (localization); $B \equiv 3\pi\hbar^2/2ma_0^2$; $g_s \equiv E_d^2/2Ca_0^3B$ is the dimensionless short-range e-ph coupling strength; and $g_l \equiv (\epsilon_s - \epsilon_\infty)e^2/\epsilon_s\epsilon_\infty a_0$ is the dimensionless long-range e-ph coupling strength, which is related to α by $\alpha = \left(\sqrt{3\pi}/2\right)(B/\hbar\omega)^{1/2}g_l$. These values of the coupling strength and the dimensionality of the system will strongly affect the behaviour of the observed carriers/excitons. Note that for excitons, $g_l = 0$ (*i.e.*, only short-range interactions are present).

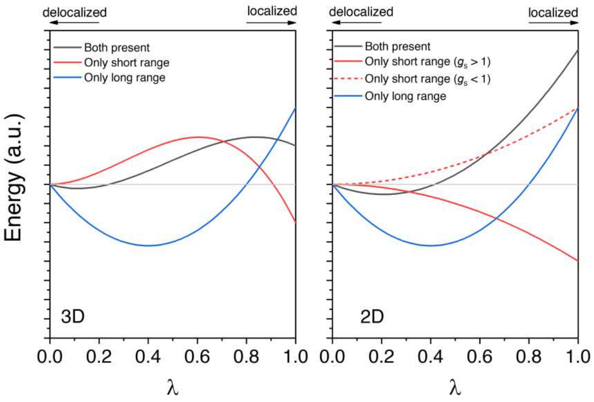

Figure 6. (a) Potential energy surface as a function of localization parameters λ for 3D and 2D systems.

To clearly visualize the contributions of the short- and long-range e-ph interactions from these equations, we plot the potential energy surfaces as function of λ for several cases (**Figure 6a**). In these plots, local energy valleys/minima indicate the most stable state of the system. From the positions of energy minima ($\lambda_{\min}$), one can deduce that the presence of long-range interactions would promote carrier delocalization for both 2D and 3D systems (*i.e.*, the energy minima fall in the range $0 < \lambda_{\min} < 1$). For excitons in 3D systems [only short-range interaction is present, red solid line in **Figure 6a** (top)], both free and self-trapped exciton could coexist with an energy barrier between them ($\lambda_{\min}$ at both 0 and 1), depending on the values of the coupling strengths. For excitons in 2D systems [only short-range interaction, red solid and dashed line in **Figure 6a** (bottom)], free and self-trapped excitons exist exclusively (only either one of them could exist at the same time), depending on whether $g_s > 1$ (self-trapped, $\lambda_{\min} = 1$) or $g_s < 1$ (free, $\lambda_{\min} = 0$).

In lead halide perovskites, while there are a lot of studies dedicated to uncovering the polaronic properties of 3D systems. Zhu, Miyata and co-workers pioneered studies of the polarons in 3D lead halide perovskites, and proposed the model of ferroelectric large polarons, where charge carriers not only distort the lattice but also trigger the formation of polar nanodomains. [90-92] On the other hand, studies on these properties in 2D RP systems are few and far between. One of the earliest indications of the polaronic nature in 2D perovskites was reported by Gauthron *et al.* [93]. From the study of the temperature-dependent broadening of the PL peak, they deduced a strong exciton-phonon coupling in $(PEA)_2PbI_4$ perovskites (n = 1), which is one order of magnitude larger than the typical values in GaAs QW systems. Wu et *al.* demonstrated the rapid localization of excitons into excitonic "puddles" by observing the blueshift of exciton resonances in transient absorption spectra of $(BA)_2(MA)_{n-1}Pb_nI_{3n+1}$ RPs (n=1, 2, 3) [94]. Specifically, the excitation energy independence of this effect was identified as a signature of strong interactions with the highly deformable environment. Furthermore, strong exciton-phonon coupling was also demonstrated by Giovanni *et al.* [76], who reported observation of coherent phonon-induced oscillation of exciton resonance energy in the same perovskite system. Recently, Zhu and co-workers demonstrated the Belgian-waffle shape of the ferroelectric polaron in 3D perovskites: where 2D sheet-like distortions cause large polaron formation in the plane and a small polaron formation in the perpendicular direction [95]. Here, the authors also proposed the possible extension of the ferroelectric large polaron model to RPs. Indeed, in 2D perovskites, stronger lattice distortion and enhanced ns^2 lone pair expression are expected to enhance local dipole moments and trigger the formation of ferroelectric polarons [95]. These studies show that the concept of polaron is indeed relevant for RP perovskite systems and we expect that future work will focus on going beyond the Fröhlich model for describing polarons in RPs.

So far, most studies on RP perovskites' polarons are focused on small exciton-polaron (*i.e.*, self-trapped exciton or STE), to tune their emission spectra for while-light emitting 2D perovskites [96, 97]. Typically, this is done by tuning the octahedral distortion of the inorganic lattice in RP perovskites, dictated by their organic spacer cation [96]. **Figure 7a** shows the mechanism of narrow absorption and broadband Stokes-shifted emission originated from self-trapped excitons for 3D semiconductors, with energy barrier between the free and self-trapped states. Such a barrier does not exist in a pure 2D case, and thus free, and self-trapped excitons are expected not to coexist [88, 89]. However, one interesting case is the 2D RP n = 1 perovskites $(PEA)_2PbCl_4$, which exhibits both free (~340 nm) and self-trapped exciton emission (broadband, peaked at ~560 nm) peaks simultaneously [98] – **Figure 7c**. This observation suggests that interlayer interactions play an important role in RP perovskites, hence retaining part of their 3D characteristics.

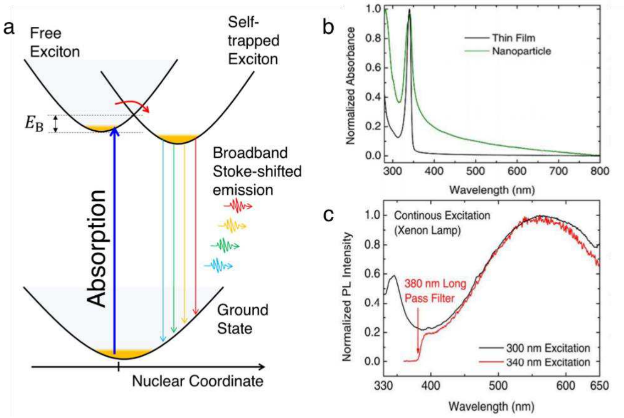

Figure 7 (a) Illustration of narrow-band absorption and broadband Stokes-shifted emission from self-trapped exciton, based on adiabatic potential energy surfaces in 3D semiconductors. (b) Absorption spectrum and (c) emission spectrum of n = 1 RP perovskite $(PEA)_2PbCl_4$, with self-trapped exciton. Figures (b) and (c) are reproduced with permission from Chem. Mater. **29**(9), 3947 (2017). Copyright 2017 American Chemical Society [98].

Usually, perovskite's excited state can be tuned towards STE making use of corrugated inorganic layers [*i.e.*, (110)-family of layered perovskites], although several exceptions of 2D perovskites with flat inorganic layers [*i.e.*, (100)-family] also shows such broadband emissions (*e.g., n* = 1 Dion-Jacobson perovskite $(EDBE)PbCl_4$ [99], or n = 1 RP perovskite $(PEA)_2PbCl_4$ [98]). For further details of white-light-emitting 2D perovskite, the reader is referred to the comprehensive review by Karunadasa *et al.* [96].

Most of the studies on polarons in RP perovskites have revolved around the fine-tuning of emission properties. Hence, the understanding of polaron effects on their transport and dynamics is relatively lacking. From the observation of a power-law dependence of the decay rate (T^{γ}, where 1.3 > γ > 1.9), Guo *et al.* [100] suggested strong electron-phonon scatterings via deformation potential by acoustic and homopolar optical phonons in $(BA)_2(MA)_{n-1}Pb_nI_{3n+1}$

(where n = 1-3). Such coupling was associated with large polaron formation with a radius extending from 10-20 lattice constants. More recently, Neutzner *et al.* [101] reported four equally-spaced features (Δ ~ 35 meV) in the exciton absorption and PL peaks in $(PEA)_2PbI_4$ n = 1 RP perovskites. Such energy spacing was estimated to be similar with polaron binding energy (with α ~ 2.2), and thus the observed features were assigned to exciton energy normalization due to polaronic effects in perovskites [101]. Polaron signatures in RP perovskites were also reported by Thouin *et al.* [102], via resonant impulsive stimulated Raman spectroscopy (RISRS) and DFT calculations, in $(PEA)_2PbI_4$ and $(BA)_2PbI_4$. Notably, these studies found that the free carrier coupling to the lattice is stronger than the excitons', as expected from the ionic nature of perovskite crystal lattice. Thouin *et al.* [103] also reported a study of population transfer between exciton fine structures, driven by strong electron-phonon coupling, in $(PEA)_2PbI_4$.

All these studies suggest that the concept of polaron is indeed relevant in discussing the excited states of RP perovskites. However, many open questions remain: *Is the polaronic nature of RP perovskites excited states beneficial/parasitic to their transport and optical properties? How does the ferroelectric nature of RPs interact with polaronic distortions? What determines the overall polaron coupling strengths and how to tune them?* These issues must be fully addressed to exploit the full potential of RP-based optoelectronic devices.

4.4. Recombination and transport dynamics

The radical changes in the electronic structure and in the nature of excitations in RPs also have profound effects on the carrier dynamics in these materials. In 3D lead halide perovskites, second order (bimolecular) radiative recombination processes underpin the slow radiative recombination observed for these materials, with lifetimes often extending up to the µs-regime.

For applications such as LEDs, where carrier injection densities are low, a slow radiative recombination can be easily outcompeted by monomolecular processes, such as trapping processes [104]. Milot *et al.* reported a thorough investigation on the recombination dynamics in $(PEA)_2(MA)_{n-1}Pb_nI_{3n+1}$ RP thin films [105]. The recombination kinetics in different mixed RP thin films was monitored for different concentration of LC in the precursor solution (*i.e.*, increasing the LC concentration reduced the average $\langle n \rangle$ value).

Notably, for high $\langle n \rangle$, the excitation dynamics reveal decreased monomolecular recombination rates k_1, thereby suggesting a trap passivation effect. As shown in **Figure 8a**, this decrease continues until equal concentrations of PEA and MA in the precursor solution, after which k_1 largely increases. Quantitatively, for MAPI the reported $k_1 = 1.3 \times 10^7$ s^{-1} decreases by almost one order of magnitude upon formation of high $\langle n \rangle$ RP phases, and ultimately increases by two order of magnitudes in PEPI for which $k_1 = 1.1 \times 10^9$ s^{-1} [105]. Beside optical probes spectroscopies, such as time-resolved photoluminescence (TRPL) and transient absorption (TA), photo-induced dynamics was studied by optical pump- THz probe (OPTP) techniques. Given that THz fields are sensitive to the movement of free charges, OPTP is used to probe the mobility (μ) of carriers in the wells [37, 105]. Mobilities resulting from OPTP are mediated by the photon-to-charge conversion efficiency (φ). Using this technique, Venkatesan *et al.* reported mobilities two-order of magnitude lower than MAPI in $(BA)_2(MA)_{n-1}Pb_nI_{3n+1}$, decreasing with lower $\langle n \rangle$.

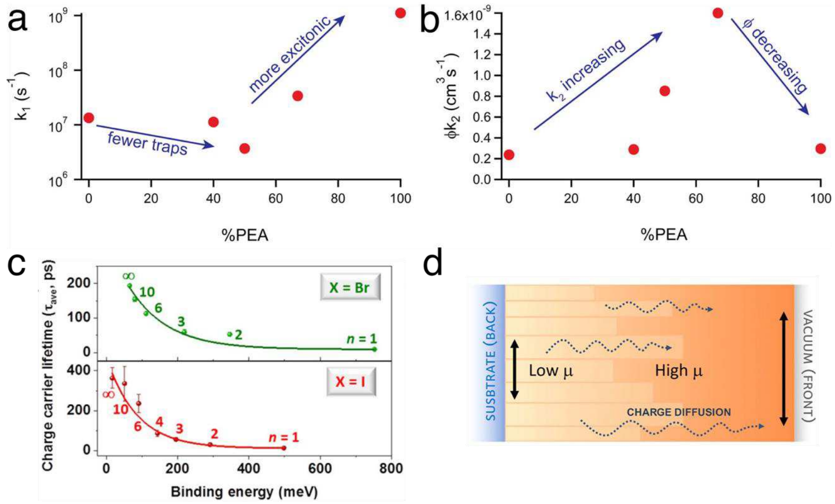

Figure 8 (a) Monomolecular recombination rate (k_1), obtained by TRPL model fitting, and (b) effective bimolecular rate constant (φk_2), obtained by OPTP model fitting, for extracted $(PEA)_2(MA)_{n-1}Pb_nI_{3n+1}$ mixed RP films. The RP thin film composition is reported as a function of PEA % concentration (*i.e.*, low PEA% corresponds to high $\langle n \rangle$, and vice versa). Milot et al. Nano Lett. **16**(11), 7001 (2016); licensed under a Creative Commons Attribution (CC BY) license [105]. (c) Charge carrier recombination lifetime (τ_{ave}) of TA bleach recoveries for $(PEA)_2(MA)_{n-1}Pb_nI_{3n+1}$ (red) and $(PEA)_2(MA)_{n-1}Pb_nBr_{3n+1}$ (green). Individual *n* phase numbers are reported in the graphic close to the data. Cho et al. J. Phys. Chem. Lett. **11**(7), 2570 (2020); licensed under a Creative Commons Attribution (CC BY) license [106]. (d) Illustration of carrier mobility mechanisms in engineered-morphology mixed RP thin films. Both charge diffusion and photon recycling are operating to transfer the population from high *n* to low *n* phases. Motti et al. Nano Lett. **19**(6), 3953 (2019); licensed under a Creative Commons Attribution (CC BY) license [107].

Also, the radiative recombination was found to be affected by the introduction of LC. Observed k_2 trends in $(PEA)_2(MA)_{n-1}Pb_nI_{3n+1}$ (**Figure 8b**) were ascribed to a decrease in the φ, as a clear proof of quantum confinement. This was recently further confirmed by Cho *et al.*: when lower $\langle n \rangle$ is considered, the increased exciton binding energy is directly related to the shorter TA lifetimes of the excited state [106]. Upon increase of PEA/MA ratio, the average lifetime of the excited state decreased from 360 to 12 ps. Similar results were observed for bromide and iodide composition of PEA-based RPs (**Figure 8c**).

Here, it is important to consider that the transformation of excited state dynamics in RPs impacts not only intrinsic aspects (*i.e.*, those outlined in **Section 4.2)** but also to extrinsic aspects. Blancon's seminal study on exfoliated RPs demonstrated the role of edge states in the ultrafast dynamics of RPs [75]. Through PL microscopy and TRPL, the authors discovered the presence of a fast internal exciton dissociation (about 200 fs) taking place at the edges of RP phases. These ultrafast-generated edge states (ES) were found to contribute to the emission spectrum of RPs with a red-shifted emission and longer PL lifetimes. Recently, Shi *et al.* shed more light on the formation of ES and on their contribution to the mobility [108]. ES formation is promoted by moisture and is therefore relevant to all applications of RPs in devices. However, different from conventional trap states, ES contribute significantly to the mobility (estimated mobilities up to 7 $cm^2 V^{-1} s^{-1}$, comparable to bulk perovskites). Also, PL dynamics studies reveal the presence of transient energies reservoirs in 2D lead halide perovskites [109]. Clearly, the relation between intrinsic and extrinsic excited state dynamics is far from being completely understood. Open questions remain that must be urgently addressed in order to establish a comprehensive understanding of RPs carrier dynamics.

From a device implementation perspective, the combination of lower mobilites and shorter lifetimes in RP, with respect to 3D LHPs, could hamper the carrier transport. While LEDs do not require ultra-long carrier transport, this is an essential requirement for perovskite based solar cells. Recently Motti *et al.*, have shown how photon recycling assists the carrier transport in these systems, by transferring the excited state population from poor conducting low *n* phases to good conductive high *n*-phases in engineered RP films (**Figure 8d**) [107]. Notably, the reported diffusion length for engineered RP systems could reach 7 μm for engineered $(BA)_x(FA_{0.83}Cs_{0.17})_{1-x}Pb(I_{0.6}Br_{0.4})_3$, and generally reach several microns for traditional RP thin films [107]. Although the role of photon recycling in RPs is fundamental [110], as confirmed by Gan *et al.*, other mechanisms of carrier diffusion are present in mixed RPs. These will be discussed in detail in the next Section.

4.5. Energy/charge funneling mechanisms: Coherent vs Incoherent transfer

From the excited state dynamics perspective, RPs exhibit a higher degree of complexity compared to bulk LHPs. Stark differences arise not only from the previously described coexistence of strongly bound excitons with free charges, edge states, and polaronic effects but also from a more complex energetic landscape [57, 111]. As described in the previous sections, the disproportionation of thicker RP phases creates mixed QW systems, where the contiguity of different RP phases results in a heterogeneous energetic landscape [28]. As a result, excited states' interactions in RPs can potentially outcompete the fast radiative recombination rates of the excitons and set the stage for inter-well migration of excited carriers [112, 113].

The thickness-dependent bandgap creates a ladder of energetic states, whereby the energetic gradient drives a funneling of excitations and carriers. Although the presence of energetic barriers and the enhancement of binding energies hamper the development of efficient solar cells, the concept of 'funneling' or 'energy cascade' has been primarily used in the field of light-emitting and has proved useful to enhance overall luminescence efficiencies [85, 111, 113-115]. Historically, the introduction of mixed RPs systems in the PeLEDs field has marked a tremendous leap in the efficiencies, reaching about 11%, with respect to the early reports of only 0.76% based on bulk perovskites [112, 113]. This field is gaining momentum and, at the moment, RP-based LEDs have reached 14.6% efficiency. Aside from the increased excitonic radiative recombination, discussed in the previous Section, the enhanced efficiencies are also attributed to the presence of this excitation funneling from lower *n* phases to higher *n* phases, where the latter act as emitters (**Figure 9a**) [111].

The nature of this cascade or funneling depends on the energy level alignment of the different RP phases. According to the Förster theory, energy transfer (here also referred to as exciton funneling, or energy cascade) can occur in the presence of an overlap between the fluorescence of the donor phase and absorption spectrum of the acceptor phase [116]. On the other hand, electron (hole) transfer can occur in the presence of different electron affinities (ionization potentials). In terms of energy level alignment, type-I heterojunctions (**Figure 9b**) promote exciton funneling from lower *n* phases to higher *n* phases, while type-II heterojunctions (**Figure 9c**) promote the separation of exciton driving electrons and holes in opposite directions [117]. Given its crucial role, the band alignment in mixed RPs is still a matter of debate within the scientific community. For example, both $(BA)_2MA_{n-1}Pb_nI_{3n+1}$ and $(PEA)_2MA_{n-1}Pb_nI_{3n+1}$ were reported to be type-I heterojunctions in some works and type-II in other works. Quintero-Bermudez *et al.* observed that surface treatments shift the work function by 1 eV, and therefore suggested that reduced ligand densities can produce band-misalignments that change the nature of the heterojunctions from an intrinsic type-I to a poor ligand density induced type-II [118]. Other possible explanations involve the "softness" of the perovskite lattice, causing a fluctuating band alignment and synthesis related inhomogeneities [117].

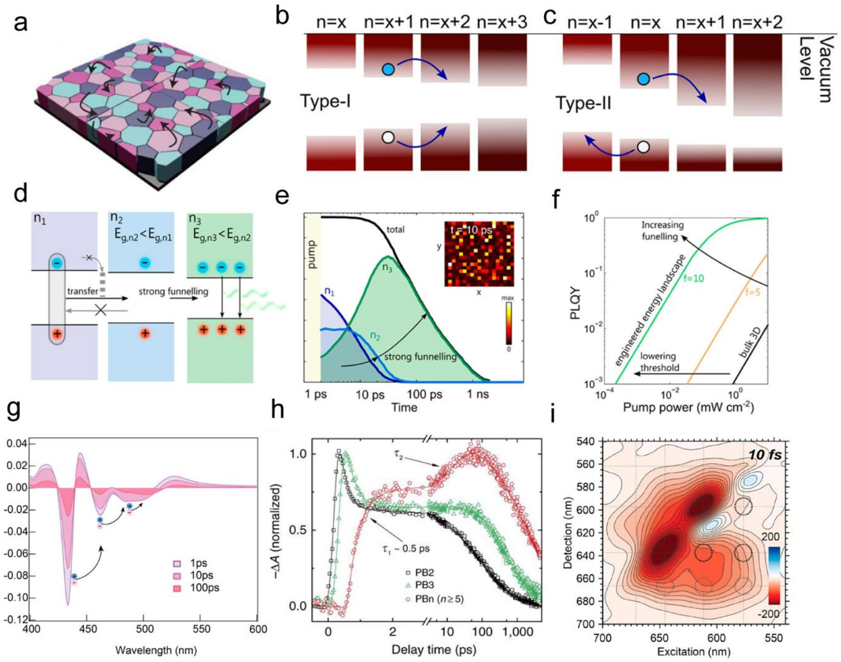

Figure 9. (a) Carrier and excitation transfer between different domains in mixed RPs systems. Reproduced with permission from Nat. Nanotech. **11**(10), 872 (2016). Copyright 2016 Nature Publishing Group [112]. (b) Type-I and (c) type-II band alignments in mixed RPs films. Due to the thickness dependent bandgap, type I alignment is expected to promote exciton transfer, while type-II alignment to promote exciton separation. Reproduced with permission from J. Am. Chem. Soc. **141**(34), 13459 (2019). Copyright 2019 American Chemical Society [118]. (d) Strong funneling from low *n*-phases can overcome trapping, and (e) cause a fast carrier concentration in low *n*-phases. (f) These high carrier concentrations boost the PL efficiencies, by increased bimolecular recombination. (g) Transient absorption photobleaching (PB) peaks can be used as a probe for the funneling, where (h) coupled growth and decay in PB signals of different *n*-phases indicate a transfer. Figure (d-g) are reproduced with permission from Nano Lett. **17**(6), 3701 (2017). Copyright 2017 American Chemical Society [111]. Figure (h) is reproduced from Xing et al. Nat. Commun. **8**(1), 14558 (2017); licensed under a Creative Commons Attribution (CC BY) license [85]. (i) Two-dimensional electronic spectroscopy maps of mixed RPs systems, where below diagonal peaks indicate an incoherent energy funneling from low to high *n*-phases in $(PEA)_2MA_{n-1}Pb_nI_{3n+1}$.

Reproduced with permission from J. Phys. Chem. Lett. **10**(3), 419 (2016). Copyright 2016 American Chemical Society [119].

While type-II alignments have been reported to enhance solar cell efficiencies, [56] there is a vast literature about finely tailored type-I RPs films to achieve efficient emission for light-emitting devices (LEDs) applications [57, 111, 112, 114]. These strategies rely on a fast transfer of excitations from highly energetic low-*n* phases, which are more prone to trapping and therefore have lower PLQYs, to the lower energetic high-*n* phases (**Figure 9d**). Thus, cascades taking place in the picosecond timescale (**Figure 9e**) can efficiently outpace trapping, thereby leading to a carrier concentration in the low-*n* phases acting as emissive sites. Notably, as shown in **Figure 9f**, carrier concentration in these phases further increases the bimolecular recombination efficiency. Although there is consensus on the excitonic nature of the transfer in bromide-based RPs, the verdict is still open for iodide-based RPs, where exciton binding energies are usually lower than bromides.

Seminal works by Sargent's group and Huang's group reported a rather complex excited state dynamics in $(PEA)_2MA_{n-1}Pb_nI_{3n+1}$ and $(NMA)_2MA_{n-1}Pb_nI_{3n+1}$ mixed RPs, respectively, resulting in an overall transfer of excited carriers from thinner to thicker phases [112, 113]. TA spectroscopy was used as a probe to characterize the funneling process. As shown in **Figure 9e**, narrow photobleaching (PB) peaks in TA spectra provide information on the specific *n*-phase population and coupled decay and rises of different PB are hallmarks of a photoinduced energy/charge transfer (**Figure 9e**). Similarly, for TRPL, the presence of PL peaks corresponding to low-n phases in the prompt PL spectrum, and their subsequent partial or full disappearance indicate an excited state interaction between the different phases. However, discriminating on the nature of this excited state interaction, whether charges or energy are transferred, is a more complicated task. As discussed in the previous section, RPs have higher EBEs, and therefore these strongly bound excitons are expected to be primary actors of this funneling. However, Jin's group reported the presence of photoinduced electron and hole separation, related to the above mentioned type-II band alignment in $(BA)_2MA_{n-1}Pb_nI_{3n+1}$ mixed RPs [43, 120]. This assignment is further substantiated in other works using two different BA isomers [121]. From a spectroscopic viewpoint, attributions to charge transfer relies on the discrepancies between rise times observed in TA and TRPL. Indeed, exciton transfer is observed in both TA and TRPL, while charge transfer still contributes to the bleaching signal of acceptor phases in TA and less to the emission signal in TRPL. Hence, longer rise times observed in the TA and absent in the TRPL, and PL decaying times of the donors not observed in the TA are used as signatures for electron and hole transfer, respectively. As reported in **Table 1**, present literature reports cascading processes on a timescale spanning four orders of magnitude (100 fs – 1 ns) and different interaction processes for similar MA lead iodide based mixed RPs. Although these apparent inconsistencies in terms of timescales and attributions may generate some confusion, the following considerations could help in rationalizing these results.

Energy and charge transfer rate constants depend on the separation *d*, between donor and acceptor QWs. The application of the Förster electronic energy transfer (EET) theory to QW systems yields an inverse quartic dependence,

$$k_{EET} \propto \frac{2\pi}{\hbar} |V_{DA}|^2 J \propto d^{-4} \tag{7}$$

where V_{DA} is the electronic coupling between the wells, and *J* the spectral overlap between the donor well emission and acceptor well absorption [122]. On the other hand, Marcus charge transfer (CT) theory usually carries a decaying exponential distance dependence, $k_{CT} \propto \exp(-\beta d)$, where β depends on the nature of the layer separating the wells [123]. Analogously to what happens in assembled nanocrystal systems, the layer of LCs separates donor and acceptor wells in RPs, therefore differently sized organic cations will modulate the coupling magnitude [28, 38, 124-127]. Accordingly, CT or charge funneling processes are reported mainly for short LC such as BA; while bulkier LCs (*e.g.*, NMA and PEA) are generally associated with EET and exciton funneling.

The inherent disorder of mixed RPs is a fundamental factor in understanding the large distribution of reported interactions timescales. Even though the relative precursors' ratios impart an overarching stoichiometry, differences in large cations solubilities and processing methods yield non-uniform phase statistics under the same average $\langle n \rangle$ value [38, 112]. Hence, given that both the number of acceptor wells weighted EET and CT contributions to the total population rate equations $k_{TOT} \propto nk_{EET} + nk_{CT}$, the observed population kinetics for each QW will vary with the distribution. Moreover, as discussed previously, different <n> values cause a completely different thin film morphology, which should be taken into account. Although more recent works always provide a series of measurements with different <n>, we believe that more systematic studies trying to isolate k_{EET} and k_{CT} are required. Notably, future systematic studies will have to consider not only compositional and morphological factors but also consider passivation, and the above-discussed possibility that imperfect passivation cause different local band-alignment, leading to carrier trapping [118, 128].

Despite occasional inconsistencies, a global pattern emerges from analysis of the timescales and assignments of the relative interaction processes (**Table 1**): interactions in the hundreds of femtoseconds timescale are generally assigned to energy transfer, while those in the hundreds of picoseconds are assigned to charge transfer. Even though, as suggested by our group, QWs in mixed RPs being statistically distributed, the presence of different distances and stacking orders could give rise to analogous processes happening over different timescales [85]. The presence of higher binding energies in RPs hinders the exciton dissociation and the subsequent charge transfer, in the absence of type-II heterojunctions. However, for practical applications in LEDs, it should be considered that the presence of electric fields could favour CT over EET, as recently demonstrated [42].

Considering that LC-driven stacking results in inter-well distances on the order of nm, the general pattern in spectroscopic results is entirely consistent with the different distance dependence of EET and CT processes mentioned above. Although ultrafast photoinduced charge transfer (~ 50 fs) have been reported for transition metal dichalcogenides QW in Van der Waals heterojunctions, and are therefore possible, these ultrafast timescales necessitate small (few Angstroms) layer separations [129]. Therefore, the nm-scale interlayer separation in RPs is expected to slow down the CT process.

Scholes *et al.* reported ultrafast interaction processes (170-230 fs) detected by means of two-dimensional electronic spectroscopy (2DES) (**Figure 9f**). This technique has already proven effective in unveiling the nature of hot and multi exciton relaxations, transfer processes and coherences in a variety of inorganic semiconductors [130-132]. The authors observe the presence of below-diagonal peaks exhibiting an ultrafast growth in $(PEA)_2MA_{n-1}Pb_nI_{3n+1}$ 2DES maps and assigned them to exciton transfer [119]. Therein, CT nonadiabatic coupling between $(PEA)_2MAPb_2I_7$ (n = 2) to $(PEA)_2MA_2Pb_3I_{10}$ (n = 3) phases, was demonstrated to be weak (about 40 meV), thereby confirming that it would proceed very slowly. On the other hand, an EET rate k_{EET} ~ 680 fs, consistent with experimental 2DES results, was obtained by estimating per the Forster theory – Eq. (7).

The presence of a strong coupling V_{DA} between excitonic transitions in RPs raises the question of whether the energy transfer regime could extend beyond the Förster regime [133]. Here, intermediate or strong coupling regimes are of particular interest, since these would potentially lead to coherent exciton transport. While the excitonic coupling is the "delocalizing force", static and dynamic disorders conspire to localize these excitons. For instance, when moved from site to site, the phonon cloud causes energy gap fluctuations and results in a "friction" against EET [134]. Excitons in QWs are generally weakly coupled to the environments (*e.g.*, the vibrational bath), as demonstrated by their characteristic narrow absorption spectrum. Hence, MQWs are ideal systems for long-range EET and possibly quantum transport. In this sense, delving deeper into the polaronic nature of excitations in RPs, as already stated in Section 4.3, becomes even more urgent. Indeed, the strong exciton-phonon coupling of LHPs, and the presence of a liquid-like structural dynamics on the 100 fs timescale, could potentially increase the friction [135]. As a result, Prezdho's group reported a rapid sub-10 fs decoherence of excitons in RPs, compared to the 20 fs reported for CdSe nanoplatelets [136, 137].

Table 1. Summary of transfer rate constant in RP perovskites. *Difference is attributed to the stacking morphology. **Extensive and more systematic study. Only selected values are presented here.

Composition	Phases involved	Time Constant	Transfer Actor	Reference
$(PEA)_2MA_{n-1}Pb_nI_{3n+1}$	2,3,4 to 5	Qualitative Interval 100 fs - 100ps	Exciton /Electron /Holes	[112]
	1 to 2	300 fs	Electron	[138]
	2 to 3	500 fs	Electron	
	3 to ∞	2.7 ps	Electron	
	1 to ∞	30 ps	Electron	

	2, 3 to $n > 10$	450 ps	Electron	[56]
	$n > 10$ to 2	400 ps	Hole	
	2 to 3	115 ± 3 ps	Exciton	[139]
	3 to 4	169 ± 8 ps	Exciton	
	4 to 5	91 ± 12 ps	Exciton	
	5 to ∞	12 ± 4 ps	Exciton	
	2 to 3*	111 ± 11 fs	Exciton	[119]
	2 to 4*	175 ± 33 ps	Exciton	
$(\mathrm{PEA})_2\mathrm{MA}_{n-1}\mathrm{Pb}_n\mathrm{Br}_{3n+1}$	2, 3, 4 to 5	Qualitative Rate ~10 ps	Exciton	[111]
$(n\text{-}\mathrm{BA})_2\mathrm{MA}_{n-1}\mathrm{Pb}_n\mathrm{I}_{3n+1}$	2, 3, 4 to ∞	477 ± 24 ps	Electron	[43]
	2 to 3	81 ± 11 ps	Electron	
	2, 3 to 4	292 ± 12 ps	Electron	
	2, 3, 4 to 5	625 ± 58 ps	Electron	
	2, 3, 4, 5 to ∞	3093 ± 143 ps	Electron	
	∞ to 4	193 ps	Hole	
	∞ to 3	987 ps	Hole	
	2 to 3	41 ± 3 ps	Electron	[120]
	2, 3 to ∞	127 ± 12 ps	Electron	
	∞ to 3	163 ± 23 ps	Hole	
	∞, 3 to 2	957 ± 19 ps	Hole	
	3 to 4, 5	350 ps	Electron	[121]
	3, 4 to 5	2.7 ns	Hole	
$(i\text{-}\mathrm{BA})_2\mathrm{MA}_{n-1}\mathrm{Pb}_n\mathrm{I}_{3n+1}$	2, 3, 4, 5 to ∞	130 ps	Electron	

	2, 3, 4, 5 to ∞	1.3 ns	Hole	
$(NMA)_2MA_{n-1}Pb_nI_{3n+1}$	2 to larger n	500 fs	Exciton	[113]
	2 to larger n	50 ps	Exciton	
	2, 3 to $n > 5$**	500 ± 100 fs	Exciton	[85]
	2, 3 to $n > 5$**	200 ± 50 ps	Exciton	
$(PBA)_2Cs_{n-1}Pb_nI_{3n+1}$	$n = 2$, 3 to $n > 4$	~ 120 fs	Exciton	[140]
	$n = 2$, 3, 4 to ∞	~ 400 fs	Exciton	

An alternative perspective on this is provided by some works supporting the presence of "static coherences", where the carrier wavefunction is delocalized along the stacking axis, and thus the presence of subbands. These subbands or miniband were hypothesized by Feldmann's group for 2D nanoplatelets assemblies [141] (*i.e.*, stacks of colloidal RP strands) and also demonstrated experimentally for RP thin films [142]. More recently, Vardeny's group supported this hypothesis using a combination of ultrafast spectroscopy and first principles calculations. Here, the authors demonstrate that excitons in PEPI are delocalized for about 10 nm in the direction perpendicular to the barriers [143]. It is noteworthy that these subbands could provide a mechanism for ultrafast and coherent energy transfer: this would be possible in mixed RPs by the excitation of a selected *n*-phase and the subsequent collapse of the delocalized wavefunction on higher n-phase at lower energy [144].

Therefore, the verdict on the possibility of coherent exciton transfer in RPs is still open, being only partially addressed by previous works. Although, we believe that cryogenic temperatures studies are strongly needed, the hunt for room temperature coherent exciton transfer continues, and will need a closer examination of the subbands hypothesis and this could possibly encompass an extension to stiffer systems such as the Dion-Jacobson perovskites.

5. RP perovskites beyond conventional optoelectronics

5.1. RP-based spintronics

Apart from the RP research for conventional optoelectronics applications (*i.e.*, PV or LEDs), one of the exciting research directions which lead-halide RPP research could take on is in emerging technology of s*pintronics*. Strong spin-orbit coupling (SOC) in lead halide perovskites (LHP), originating from its heavy element component such as Pb, offers control access to the materials' spin degree of freedom via structural (*e.g.*, Rashba effect [145, 146]) or optical means (*e.g.* spin-polarized excitation/emission [147-150]). SOC hybridizes both the *p*-like conduction and *s*-like valence band-edges of the lead halide perovskites with the electron's S = 1/2 spin-states, resulting in doubly degenerate J = 1/2 total angular momentum states (or *J*-states) with azimuthal quantum number m_j = ±1/2 (**Figure 10a**).

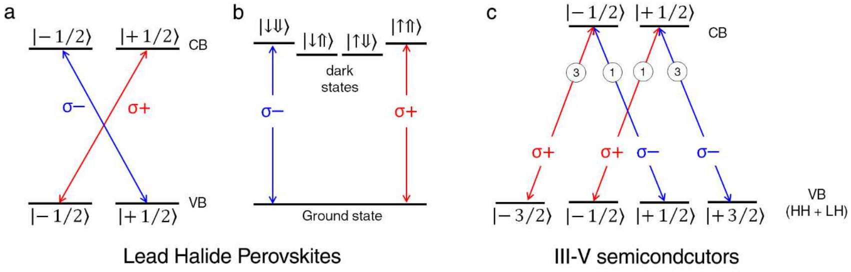

Figure 10 (a) Optical selection rules based on electron total angular momentum states of $|\boldsymbol{m_j}\rangle$ of the perovskite band-edges. CB and VB correspond to the conduction and valence band, respectively. (b) Optical selection rules for exciton in perovskites. The ↑ and ↓ represents electron's spin-up and spin-down states, respectively, while ⇓ and ⇑ represents hole's spin-up and spin-down states, respectively. (c) The selection rule for conventional III-V and II-VI semiconductors' band-edges. The HH and LH refers to the heavy-hole and light-hole band, respectively.

For the case of an exciton, where the electron and holes are bound together by Coulombic interaction, these *J*-states further hybridize into 4 states, *i.e.*, two bright exciton states: $|+1\rangle$ (or $|\uparrow\Uparrow\rangle$) and $|-1\rangle$ (or $|\downarrow\Downarrow\rangle$) states, and two dark exciton states: $|\downarrow\Uparrow\rangle$ and $|\uparrow\Downarrow\rangle$ [69, 151]. The single (↑ and ↓) and double (⇑ and ⇓) arrows represent the electron and hole *J*-states (or hereafter loosely referred as "spin"), respectively (**Figure 10b**). Such unusual electronic structure results in the optical selection rules as shown in **Figure 10a-b**. Excitation by circularly polarized light results in 100% spin-polarization, to be contrasted from the conventional III-V or II-VI semiconductors (*e.g.*, GaAs, InAs, CdTe, etc.), where circular-polarized excitation only yields 50% spin-polarization [152] – **Figure 10c**. One of the earliest reports which highlights the potential of LHP was the demonstration of ultra-large photoinduced Faraday rotation in the 3D $MAPbI_3$ perovskite by Giovanni *et al.* [147], followed by the report on magnetic-field-induced spin-mixing in the same perovskite system by Zhang *et al.* [150]. Following those two earliest studies, follow-up works have demonstrated various spin phenomena across different perovskite systems. Several works to be highlighted include experimental demonstration of quantum spin-beating [153, 154], spin-selective optical Stark effect [155, 156], Rashba effect [143, 157], and perovskite based spin-valves [149, 158, 159].

While most of these studies were focused on the 3D LHP systems, several studies have also demonstrated the prospect of RP for spintronic applications. Giovanni *et al.* [155] reported the observation of tunable spin-selective optical Stark effect (OSE) in $n = 1$ RPP thin films (**Figure 11a**). OSE is a 3rd-order nonlinear process where the exciton energy is blue-shifted due to interaction with photon with energy below the excitonic resonance. It provides a measure of the Rabi energy, which characterizes the strength of light-matter coupling in a material. Here, the interaction between the photon and the exciton $|\pm1\rangle$ spin states could selectively be controlled by using the photon helicity. **Figure 11a** shows differential-like transient absorption spectra of $(PEA)_2PbI_4$ thin film (*i.e.*, PEA = phenylethylammonium), signifying a blue shift, which depends on the pump and probe circular helicity and only occurs during laser pulse duration, where little to none of the population from multi-photon absorption is involved. Such ultrafast process holds prospective applications for opto-spin logic devices in quantum information. This study also found that this spin-selective Rabi energy in RPP could easily be tuned by controlling the dielectric contrast between the organic and inorganic layer and is several times larger than what was found in the conventional III-V or II-VI inorganic semiconductors, thus highlighting the superiority of RPP for opto-spintronic applications.

Meanwhile, most studies have focused on the Rashba effects in RP. Rashba effect is the splitting of the spin-dependent (*i.e.*, spin-up and spin-down) energy dispersion $E(k)$ in momentum, observed only in non-centrosymmetric material systems (**Figure 11b**). In the parabolic band approximation, the ±½ spin-band can be mathematically described as $E(k) = (\hbar^2 k^2/2m^*) \pm \alpha_R|k|$; where m^* is the effective mass, and α_R is the Rashba parameters. The momentum offset (k_0) and energy barrier between the two spin bands (E_R) are related to α_R by $k_0 = m^*\alpha_R/\hbar^2$ and $E_R = \alpha_R k_0/2$. Rashba effect provides control access of spin degree of freedom in the material, through the manipulation of the material's structure (*e.g.*, via pressure [160] or electric field [145]), which is crucial for the realization of spintronic technology.

Zhai *et al.* [143] reports the observation of giant Rashba splitting in *n* = 1 $(PEA)_2PbI_4$ RP films, via ultra-broadband ultrafast and steady-state transient absorption (or photomodulation, PM) spectroscopy. **Figure 11c** shows the ultrafast and steady-state PM spectra of $(PEA)_2PbI_4$ thin film, where the former shows a photoinduced absorption peak (PA1) at 0.35 eV, while the latter shows a free-carrier absorption (FCA) peak at 0.15 eV. These two peaks were assigned to optical transition from the 1s exciton state and continuum band-edge to Rashba split band, respectively. From these transitions, they derived $E_R = 40 \pm 5$ meV and $\alpha_R = (1.6 \pm 0.1)$ eV·Å, whose values were among the largest value of Rashba splitting reported so far.

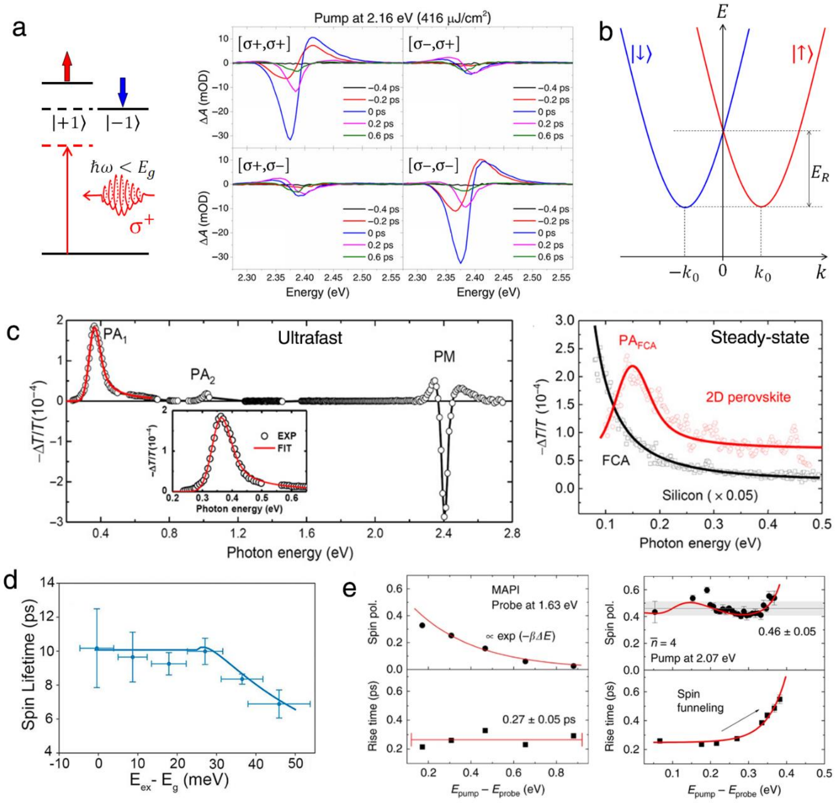

Figure 11. (a) Spin-selective optical Stark effect (OSE) in n = 1 $(PEA)_2PbI_4$ film. Illustration of spin-selective OSE, spectral features, and dynamics are shown. Giovanni et al. Sci. Adv. **2**(6), (2016); licensed under a Creative Commons Attribution (CC BY) license [155]. (b) Illustration of the Rashba effect. (c) Broadband ultrafast and steady-state photo modulation spectra of the n = 1 $(PEA)_2PbI_4$ film. Figure (b)-(c) are reproduced from Zhai et al. Sci. Adv. **3**(7), (2017); licensed under a Creative Commons Attribution (CC BY) license [143]. (d) Measured exciton spin lifetime in n = 2 $(BA)_2Pb_2I_7$ film as function of excess excitation energy. Todd et al. APL Mater. **7**(8), (2019); licensed under a Creative Commons Attribution (CC BY) license [157]. (e) Spin funnelling in mixed-phase $(\mathrm{PEA})_2(\mathrm{MA})_{n-1}\mathrm{Pb}_n\mathrm{I}_{3n+1}$ RP films. Spin polarization and funnelling time at different phases as a function

of excess excitation energy for 3D $MAPbI_3$ (MAPI) and RPP films, are shown. Giovanni et al. Nat. Commun. **10**(1), (2019); licensed under a Creative Commons Attribution (CC BY) license [44].

Rashba effect was also found to affect the spin dynamics in RPs. Chen *et al.* [148] discovered that the spin longitudinal lifetime (T_1) of excitons in $(PEA)_2(MA)_{n-1}Pb_nI_{3n+1}$ single crystals increases with increasing phase number n (up to $n = 4$), but drops back for the case of 3D perovskites. This peculiar behaviour was assigned to an interplay between phonon scatterings and Rashba effect. Todd *et al.* [157] reports the decrease of T_1 as function as excess excitation energy in $(BA)_2(MA)Pb_2I_7$ RP thin films. By using Rashba precession spin relaxation model, the T_1 trend could quantitatively be explained (**Figure 11d**), and Rashba parameter $\alpha_R = 0.08$ eV·Å was derived. The discrepancy from the previous result by Zhai *et al.* [143] was assigned to the different LC used in the study – implying the tuning of the Rashba effect by simply playing with the chemistry of RP.

Recently, another demonstration RPs' potential for spintronics was reported by Giovanni *et al.* [44], where a ultrafast spin funnelling from high bandgap to low bandgap phases in mixed RP films was reported. **Figure 11e** shows the distribution of exciton spin polarization and signal rise time of $MAPbI_3$ and mixed RP thin film, as a function of pump-probe energy detuning, measured by transient absorption technique. The spin polarization trend observed in RP is different from the typical exponential decay -trend observed in common semiconductors (*e.g.* in $MAPbI_3$), were the spin transport is limited by momentum scattering. Instead, such trend is well-described by trap-limited energy funneling model, which signifies the presence of an ultrafast spin funneling process in mixed RPs. Utilizing this idea, room-temperature unidirectional longitudinal spin funnelling across film thickness of ~600 nm was demonstrated in engineered graded 2D/3D RP films, which could reinvigorate the concepts of spin-information transfer.

Recently, a new development in perovskite-based spintronics which takes on an interesting twist is chiral perovskites [161, 162]. Using chiral organic molecules as its organic spacer layer, Long *et al.* [162] demonstrated strong circular dichroism and 3% intrinsic spin-polarized PL in the absence of magnetic field at 77 K, in a mixed dimension $(R/S\text{-MBA})_2(\text{MA})_{n-1}\text{Pb}_n\text{Br}_{3n+1}$ systems (MBA = methylbenzylamine). Using a similar concept in the same system ($n = 1$), Lu *et al.* [161] demonstrated spin-selectivity of out-of-plane electron transport, depending on the chirality of the organic molecules. These two studies suggest that the spin-degeneracy in RP perovskites were lifted due to the introduction of chiral molecules. The physics behind this observation requires further clarifications [161].

These studies have so far indicated RP as an ideal material system for exploiting new breakthroughs in semiconductor spintronics, which hitherto have seen only limited success in solution-processed organic systems. However, given the current understanding on the spin-physics in RP, it is fair to say that this field is still at its infancy. Many open questions, for instance: the role of RP's dimensionality and large cations for the spin physics, the spin funneling and relaxation mechanisms, the spin transport mechanisms and properties, *etc.*; have to be first answered before one could embark on designing a working RP-based spin device architecture. What's next would be the call for spectroscopists to answer these lingering questions to build a solid understanding of the spin physics in RP.

5.2. Tuning of band offset and interlayer interactions in RPs

LC engineering could help RP to transcend their limitations, using the MQW as a flexible platform where the electronic bands and the interlayer interactions are tailored. The possibility of playing with the internal band alignments (*i.e.*, the electronic band of the LC layer and the inorganic layer) has already been explored in the 90s. Again, Mitzi *et al.* [163] were the first to introduce a conjugated molecule (AEQT, a diammonium quatertiophene) as a LC and to observe strong emission from the LC. A few years later, Zhu *et al.* [164] further developed this concept and reported difficulties in forming RP structures with monoammonium LC for large conjugated molecules, as compared to diammonium LCs. In recent years, the interest for these complex RP structure has surged [165, 166]. Gao *et al.* [167] fabricated crystalline RPs using a series of oligotiophene LC with decreasing HOMO-LUMO levels. The resulting RPs show increasingly redshifted emission, as a signature of quasi-Type II, type-II, and inverted type-I heterostructures. This was further confirmed by first principle calculations. It is worth stressing here that this band alignment refers to the organic and inorganic part of the RP structure, and not to the inter-well alignment in mixed RPs (discussed in **Section 4.5**). A fundamental difference lies in the timescales for internal charge separation. While these timescale lies in the hundreds of picoseconds for inter-well CT (Table 1), recently Gélvez-Rueda *et al.* [168] demonstrated that it is possible to extract photoexcited holes to an organic LC in colloidal RPs within 1 ps. The frontier of this research was further advanced in the past year, with the development of a comprehensive first-principle calculations [169], a synthetic deposition strategy (*i.e.*, resonant infrared matrix- assisted pulsed laser evaporation, RIR-MAPLE), and the first ultrafast dynamics studies, validating the band alignment, by Mitzi's group [169, 170]. These studies demonstrate the huge potential of LC engineering to create tailored RP beyond the traditional MQW, we expect this field of research to flourish over the next few years. The field could also be further boosted by the introduction of simulations and accurate modelling that provide guidance for the tuning of the complex interplay of interactions.

6. Conclusion and Prospects for RP research

In retrospect, we have described the burgeoning development of RPs in the past lustrum and the exciting opportunities ahead. As outlined in this review, their potential goes well beyond the initial excitement for increased stability with respect to bulk lead halide perovskites. Possible development areas are cross-sectorial and range from their structure, morphology and understanding of their photophysical properties. It is very clear that a multi-disciplinary approach is the key to enable exciting developments outlined in this review. For instance, the challenge of achieving a finely tuned (and possibly coherent) transport across the QW in mixed RPs, outlined in **Section 4.5**, will not only require a deeper understanding of this phenomenon but must also be expediated by advancements in the synthetic control of the Structure (**Section 2.1**) and Morphology (**Section 2.2**). Here, achieving a tailored, well-oriented, and possibly stiffer structures by controlling the types of LCs and the fabrication methodologies/strategies will promote coherent delocalization of excitons. In this context, multidimensional spectroscopic techniques, such as 2DES and other physical property characterization techniques like in-situ synchrotron-based X-ray diffraction, ultrafast electron microscopy *etc.*, will provide further guidance.

Hence, mixed RPs emerge as exceptional optoelectronic platforms for device applications. The toolbox developed during these years will prove extremely useful in solving open challenges to maximize their performances. A fine-tuning of the band alignment toward type-II heterojunctions between QW will help to foster solar cell efficiencies and reach performances comparable to that of bulk perovskites. For LEDs application, a deeper understanding of inter-well transport (*i.e.*, balanced electron and hole transfer will be advantageous) and the mechanisms of efficiency roll-off (*i.e.*, charge or exciton annihilation) are urgently needed. Here, developing mixed electrical and optical measurements, such as electric field assisted ultrafast spectroscopies, is paramount for both materials and device advancements. These applications will also benefit from increased understanding on the nature of excited species (**Section 4**). Many open questions on the balance of free carrier and excitons in RPs, and the contextual role of exciton-phonon interactions remain to be addressed.

Here, RPs are also excellent candidates to spur the development of novel physics concepts such as the optical control of spin in inorganic materials. Albeit the exciting results presented here, this field is still in its infancy, and we expect new studies to be flourishing. As mentioned in **Section 5**, roles of LC and dimensionality are still be investigated. Combining these advancements with those in the control of energy and charge cascades, finely tuned spin funnels could be tailored for spintronics application. In this regard, the flexibility of RPs chemistry opens to the possibility of doping these materials with magnetic ions or coupling them with materials with excellent spin transport properties. Are these versatile multi-dimensional RP perovskites the future of perovskite optoelectronics, the world wonders ……

Acknowledgements

This research was supported by Nanyang Technological University under its start-up grant (M4080514); the Ministry of Education under its AcRF Tier 1 grant (RG91/19) and Tier 2 grants (MOE2017-T2-1-001, MOE2017-T2-2-002 and MOE2019-T2-1-006); and the National Research Foundation (NRF) Singapore under its Competitive Research Program (NRF-CRP14-2014-03) and NRF Investigatorship (NRF-NRFI-2018-04).

Data Availability Statement

The data that support the findings of this study are available from the corresponding author upon reasonable request.

References

1. Jena, A.K., A. Kulkarni, and T. Miyasaka, *Halide perovskite photovoltaics: background, status, and future prospects.* Chemical Reviews, 2019. **119**(5): p. 3036-3103.
2. Snaith, H.J., *Present status and future prospects of perovskite photovoltaics.* Nature Materials, 2018. **17**(5): p. 372-376.
3. Veldhuis, S.A., et al., *Perovskite Materials for Light-Emitting Diodes and Lasers.* Advanced Materials, 2016. **28**(32): p. 6804-6834.
4. Li, M., et al., *Slow hot-carrier cooling in halide perovskites: prospects for hot-carrier solar cells.* Advanced Materials, 2019. **31**(47): p. 1802486.
5. Lim, J.W.M., et al., *Hot carriers in halide perovskites: how hot truly?* The Journal of Physical Chemistry Letters, 2020. **11**(7): p. 2743-2750.
6. Utzat, H., et al., *Coherent single-photon emission from colloidal lead halide perovskite quantum dots.* Science, 2019. **363**(6431): p. 1068.
7. Righetto, M., et al., *Coupling halide perovskites with different materials: From doping to nanocomposites, beyond photovoltaics.* Progress in Materials Science, 2020. **110**: p. 100639.
8. Manser, J.S., J.A. Christians, and P.V. Kamat, *Intriguing optoelectronic properties of metal halide Perovskites.* Chemical Reviews, 2016. **116**(21): p. 12956-13008.
9. Kieslich, G., S. Sun, and A.K. Cheetham, *An extended Tolerance Factor approach for organic–inorganic perovskites.* Chemical Science, 2015. **6**(6): p. 3430-3433.
10. Bonn, M., et al., *Role of dielectric drag in polaron mobility in lead halide perovskites.* ACS Energy Letters, 2017. **2**(11): p. 2555-2562.

11. Taylor, V.C.A., et al., *Investigating the role of the organic cation in formamidinium lead iodide perovskite using ultrafast spectroscopy.* The Journal of Physical Chemistry Letters, 2018. **9**(4): p. 895-901.

12. Xiao, Z., et al., *Searching for promising new perovskite-based photovoltaic absorbers: the importance of electronic dimensionality.* Materials Horizons, 2017. **4**(2): p. 206-216.

13. Zhao, X.-G., et al., *Rational design of halide double perovskites for optoelectronic applications.* Joule, 2018. **2**(9): p. 1662-1673.

14. Meggiolaro, D., et al., *Iodine chemistry determines the defect tolerance of lead-halide perovskites.* Energy & Environmental Science, 2018. **11**(3): p. 702-713.

15. Xing, G., et al., *Long-Range Balanced Electron- and Hole-Transport Lengths in Organic-Inorganic CH<sub>3</sub>NH<sub>3</sub>PbI<sub>3</sub>.* Science, 2013. **342**(6156): p. 344.

16. Stranks, S.D., et al., *Electron-Hole Diffusion Lengths Exceeding 1 Micrometer in an Organometal Trihalide Perovskite Absorber.* Science, 2013. **342**(6156): p. 341.

17. Green, M.A., A. Ho-Baillie, and H.J. Snaith, *The emergence of perovskite solar cells.* Nature Photonics, 2014. **8**(7): p. 506-514.

18. Miyata, A., et al., *Direct measurement of the exciton binding energy and effective masses for charge carriers in organic–inorganic tri-halide perovskites.* Nature Physics, 2015. **11**(7): p. 582-587.

19. Yablonovitch, E., O.D. Miller, and S.R. Kurtz, *A great solar cell also needs to be a great LED: External fluorescence leads to new efficiency record.* AIP Conference Proceedings, 2013. **1519**(1): p. 9-11.

20. Cao, D.H., et al., *2D homologous perovskites as light-absorbing materials for solar cell applications.* Journal of the American Chemical Society, 2015. **137**(24): p. 7843-7850.

21. Kagan, C.R., D.B. Mitzi, and C.D. Dimitrakopoulos, *Organic-inorganic hybrid materials as semiconducting channels in thin-film field-effect transistors.* Science, 1999. **286**(5441): p. 945.

22. Smith, I.C., et al., *A layered hybrid perovskite solar-cell absorber with enhanced moisture stability.* Angewandte Chemie International Edition, 2014. **53**(42): p. 11232-11235.

23. Mao, L., C.C. Stoumpos, and M.G. Kanatzidis, *Two-dimensional hybrid halide perovskites: principles and promises.* Journal of the American Chemical Society, 2019. **141**(3): p. 1171-1190.

24. Saparov, B. and D.B. Mitzi, *Organic-inorganic perovskites: structural versatility for functional materials design.* Chemical Reviews, 2016. **116**(7): p. 4558-4596.

25. Zheng, H., et al., *The effect of hydrophobicity of ammonium salts on stability of quasi-2D perovskite materials in moist condition.* Advanced Energy Materials, 2018. **8**(21): p. 1800051.

26. Quan, L.N., et al., *Ligand-Stabilized Reduced-Dimensionality Perovskites.* Journal of the American Chemical Society, 2016. **138**(8): p. 2649-2655.

27. Soe, C.M.M., et al., *Structural and thermodynamic limits of layer thickness in 2D halide perovskites.* Proceedings of the National Academy of Sciences, 2019. **116**(1): p. 58.

28. Stoumpos, C.C., et al., *High members of the 2D Ruddlesden-Popper halide perovskites: synthesis, optical Properties, and solar cells of* $(CH_3(CH_2)_3NH_3)_2(CH_3NH_3)_4Pb_5I_{16}$. Chem, 2017. **2**(3): p. 427-440.

29. Li, C., et al., *Formability of* ABX_3 *(X = F, Cl, Br, I) halide perovskites.* Acta Crystallographica Section B, 2008. **64**(6): p. 702-707.

30. Mitzi, D.B., *Templating and structural engineering in organic–inorganic perovskites.* Journal of the Chemical Society, Dalton Transactions, 2001(1): p. 1-12.

31. Mitzi, D.B., C.D. Dimitrakopoulos, and L.L. Kosbar, *Structurally Tailored Organic−Inorganic Perovskites: Optical Properties and Solution-Processed Channel Materials for Thin-Film Transistors.* Chemistry of Materials, 2001. **13**(10): p. 3728-3740.

32. Mitzi, D.B., D.R. Medeiros, and P.R.L. Malenfant, *Intercalated Organic−Inorganic Perovskites Stabilized by Fluoroaryl−Aryl Interactions.* Inorganic Chemistry, 2002. **41**(8): p. 2134-2145.

33. Xiao, Z., et al., *Defect properties of the two-dimensional (CH3NH3)2Pb(SCN)2I2 perovskite: a density-functional theory study.* Physical Chemistry Chemical Physics, 2016. **18**(37): p. 25786-25790.

34. Xiao, Z., et al., *Photovoltaic Properties of Two-Dimensional (CH3NH3)2Pb(SCN)2I2 Perovskite: A Combined Experimental and Density Functional Theory Study.* The Journal of Physical Chemistry Letters, 2016. **7**(7): p. 1213-1218.

35. Calabrese, J., et al., *Preparation and characterization of layered lead halide compounds.* Journal of the American Chemical Society, 1991. **113**(6): p. 2328-2330.

36. Ishihara, T., J. Takahashi, and T. Goto, *Exciton state in two-dimensional perovskite semiconductor* $(C_{10}H_{21}NH_3)_2PbI_4$. Solid State Communications, 1989. **69**(9): p. 933-936.

37. Venkatesan, N.R., et al., *Phase intergrowth and structural defects in organic metal halide Ruddlesden–Popper thin films.* Chemistry of Materials, 2018. **30**(23): p. 8615-8623.

38. Quintero-Bermudez, R., et al., *Compositional and orientational control in metal halide perovskites of reduced dimensionality.* Nature Materials, 2018. **17**(10): p. 900-907.

39. Tsai, H., et al., *High-efficiency two-dimensional Ruddlesden–Popper perovskite solar cells.* Nature, 2016. **536**(7616): p. 312-316.

40. Stoumpos, C.C., et al., *Ruddlesden–Popper Hybrid Lead Iodide Perovskite 2D Homologous Semiconductors.* Chemistry of Materials, 2016. **28**(8): p. 2852-2867.

41. Soe, C.M.M., et al., *Understanding film formation morphology and orientation in high member 2D Ruddlesden–Popper perovskites for high-efficiency solar cells.* Advanced Energy Materials, 2018. **8**(1): p. 1700979.

42. Cheng, P., et al., *Highly efficient Ruddlesden-Popper halide perovskite* $PA_2MA_4Pb_5I_{16}$ *Solar Cells.* ACS Energy Letters, 2018. **3**(8): p. 1975-1982.

43. Liu, J., et al., *Observation of internal photoinduced electron and hole separation in hybrid two-dimentional perovskite films.* Journal of the American Chemical Society, 2017. **139**(4): p. 1432-1435.

44. Giovanni, D., et al., *Ultrafast long-range spin-funneling in solution-processed Ruddlesden–Popper halide perovskites.* Nature Communications, 2019. **10**(1): p. 3456.

45. Wang, J., et al., *Templated growth of oriented layered hybrid perovskites on 3D-like perovskites.* Nature Communications, 2020. **11**(1): p. 582.

46. Zhang, J., et al., *Binary solvent engineering for high-performance two-dimensional perovskite solar cells.* ACS Sustainable Chemistry & Engineering, 2019. **7**(3): p. 3487-3495.

47. Fu, W., et al., *Two-dimensional perovskite solar cells with 14.1% power conversion efficiency and 0.68% external radiative efficiency.* ACS Energy Letters, 2018. **3**(9): p. 2086-2093.

48. Xu, H., et al., *Orientation regulation of tin-based reduced-dimensional perovskites for highly efficient and stable photovoltaics.* Advanced Functional Materials, 2019. **29**(47): p. 1807696.

49. Zhang, X., et al., *Orientation regulation of phenylethylammonium cation based 2D perovskite solar cell with efficiency higher than 11%.* Advanced Energy Materials, 2018. **8**(14): p. 1702498.

50. Lai, H., et al., *Two-dimensional Ruddlesden–Popper perovskite with nanorod-like morphology for solar cells with efficiency exceeding 15%.* Journal of the American Chemical Society, 2018. **140**(37): p. 11639-11646.

51. Zhang, Y., et al., *Highly efficient guanidinium-based quasi 2D perovskite solar cells via a two-step post-treatment process.* Small Methods, 2019. **3**(11): p. 1900375.

52. Zhou, N., et al., *Exploration of crystallization kinetics in quasi two-dimensional perovskite and high performance solar cells.* Journal of the American Chemical Society, 2018. **140**(1): p. 459-465.

53. Chen, A.Z., et al., *Origin of vertical orientation in two-dimensional metal halide perovskites and its effect on photovoltaic performance.* Nature Communications, 2018. **9**(1): p. 1336.

54. Chen, A.Z., et al., *Understanding the formation of vertical orientation in two-dimensional metal halide perovskite thin films.* Chemistry of Materials, 2019. **31**(4): p. 1336-1343.

55. Zhang, F., et al., *Advances in two-dimensional organic–inorganic hybrid perovskites.* Energy & Environmental Science, 2020. **13**(4): p. 1154-1186.

56. Qing, J., et al., *Aligned and Graded Type-II Ruddlesden–Popper Perovskite Films for Efficient Solar Cells.* Advanced Energy Materials, 2018. **8**(21): p. 1800185.

57. Yantara, N., et al., *Designing efficient energy funneling kinetics in Ruddlesden–Popper perovskites for high-performance light-emitting diodes.* Advanced Materials, 2018. **30**(33): p. 1800818.

58. Liu, X.-K. and F. Gao, *Organic–Inorganic Hybrid Ruddlesden–Popper Perovskites: An Emerging Paradigm for High-Performance Light-Emitting Diodes.* The Journal of Physical Chemistry Letters, 2018. **9**(9): p. 2251-2258.

59. Filip, M.R., C. Verdi, and F. Giustino, *GW band structures and carrier effective masses of $CH_3NH_3PbI_3$ and hypothetical perovskites of the type $APbI_3$: A = NH_4, PH_4, AsH_4, and SbH_4.* The Journal of Physical Chemistry C, 2015. **119**(45): p. 25209-25219.

60. Caputo, M., et al., *Electronic structure of $MAPbI_3$ and $MAPbCl_3$: importance of band alignment.* Scientific Reports, 2019. **9**(1): p. 15159.

61. Tanaka, K. and T. Kondo, *Bandgap and exciton binding energies in lead-iodide-based natural quantum-well crystals.* Science and Technology of Advanced Materials, 2003. **4**(6): p. 599-604.

62. Umebayashi, T., et al., *Electronic structures of lead iodide based low-dimensional crystals.* Physical Review B, 2003. **67**(15): p. 155405.

63. Even, J., L. Pedesseau, and C. Katan, *Understanding quantum confinement of charge carriers in layered 2D hybrid perovskites.* ChemPhysChem, 2014. **15**(17): p. 3733-3741.

64. Ishihara, T., et al., *Dielectric confinement effect for exciton and biexciton states in PbI_4-based two-dimensional semiconductor structures.* Surface Science, 1992. **267**(1): p. 323-326.

65. Hong, X., T. Ishihara, and A.V. Nurmikko, *Dielectric confinement effect on excitons in ${\mathrm{PbI}}_{4}$-based layered semiconductors.* Physical Review B, 1992. **45**(12): p. 6961-6964.

66. Traore, B., et al., *Composite nature of layered hybrid perovskites: assessment on quantum and dielectric confinements and band alignment.* ACS Nano, 2018. **12**(4): p. 3321-3332.

67. Katan, C., N. Mercier, and J. Even, *Quantum and dielectric confinement effects in lower-dimensional hybrid perovskite semiconductors.* Chemical Reviews, 2019. **119**(5): p. 3140-3192.

68. Pedesseau, L., et al., *Advances and promises of layered halide hybrid perovskite semiconductors.* ACS Nano, 2016. **10**(11): p. 9776-9786.

69. Tanaka, K., et al., *Comparative study on the excitons in lead-halide-based perovskite-type crystals $CH_3NH_3PbBr_3$ $CH_3NH_3PbI_3$.* Solid State Communications, 2003. **127**(9): p. 619-623.

70. Blancon, J.C., et al., *Scaling law for excitons in 2D perovskite quantum wells.* Nature Communications, 2018. **9**(1): p. 2254.

71. Marongiu, D., et al., *The role of excitons in 3D and 2D lead halide perovskites.* Journal of Materials Chemistry C, 2019. **7**(39): p. 12006-12018.

72. Yaffe, O., et al., *Excitons in ultrathin organic-inorganic perovskite crystals.* Physical Review B, 2015. **92**(4): p. 045414.

73. Mitzi, D.B., et al., *Conducting tin halides with a layered organic-based perovskite structure.* Nature, 1994. **369**(6480): p. 467-469.

74. Papavassiliou, G.C. and I.B. Koutselas, *Structural, optical and related properties of some natural three- and lower-dimensional semiconductor systems.* Synthetic Metals, 1995. **71**(1): p. 1713-1714.

75. Blancon, J.C., et al., *Extremely efficient internal exciton dissociation through edge states in layered 2D perovskites.* Science, 2017. **355**(6331): p. 1288.

76. Giovanni, D., et al., *Coherent spin and quasiparticle dynamics in solution-processed layered 2D lead halide perovskites.* Advanced Science, 2018. **5**(10): p. 1800664.

77. Sarritzu, V., et al., *Perovskite excitonics: primary exciton creation and crossover from free carriers to a secondary exciton phase.* Advanced Optical Materials, 2018. **6**(3): p. 1700839.

78. Richter, J.M., et al., *Ultrafast carrier thermalization in lead iodide perovskite probed with two-dimensional electronic spectroscopy.* Nature Communications, 2017. **8**(1): p. 376.

79. Hintermayr, V.A., et al., *Accelerated carrier relaxation through reduced Coulomb screening in two-dimensional halide perovskite nanoplatelets.* ACS Nano, 2018. **12**(10): p. 10151-10158.

80. Yin, J., et al., *Tuning hot carrier cooling dynamics by dielectric confinement in two-dimensional hybrid perovskite crystals.* ACS Nano, 2019. **13**(11): p. 12621-12629.

81. Sheng, C., et al., *Exciton versus free carrier photogeneration in organometal trihalide perovskites probed by broadband ultrafast polarization memory dynamics.* Physical Review Letters, 2015. **114**(11): p. 116601.

82. D'Innocenzo, V., et al., *Excitons versus free charges in organo-lead tri-halide perovskites.* Nature Communications, 2014. **5**(1): p. 3586.

83. Wang, W., et al., *Density-dependent dynamical coexistence of excitons and free carriers in the organolead perovskite $CH_3NH_3PbI_3$.* Physical Review B, 2016. **94**(14): p. 140302.

84. Gélvez-Rueda, M.C., et al., *Interconversion between Free Charges and Bound Excitons in 2D Hybrid Lead Halide Perovskites.* The Journal of Physical Chemistry C, 2017. **121**(47): p. 26566-26574.

85. Xing, G., et al., *Transcending the slow bimolecular recombination in lead-halide perovskites for electroluminescence.* Nature Communications, 2017. **8**(1): p. 14558.

86. Cingolani, R., et al., *Radiative recombination processes in wide-band-gap II–VI quantum wells: the interplay between excitons and free carriers.* Journal of the Optical Society of America B, 1996. **13**(6): p. 1268-1277.

87. Sekiguchi, F. and R. Shimano, *Rate equation analysis of the dynamics of first-order exciton Mott transition.* Journal of the Physical Society of Japan, 2017. **86**(10): p. 103702.

88. Song, K. and R.T. Williams, *Self-trapped excitons*. Vol. 105. 1993: Springer Science & Business Media.

89. Ueta, M., et al., *Excitonic processes in solids*. Vol. 60. 1986: Springer Science & Business Media.

90. Joshi, P.P., S.F. Maehrlein, and X. Zhu, *Dynamic Screening and Slow Cooling of Hot Carriers in Lead Halide Perovskites.* Advanced Materials, 2019. **31**(47): p. 1803054.

91. Miyata, K. and X.Y. Zhu, *Ferroelectric large polarons.* Nature Materials, 2018. **17**(5): p. 379-381.

92. Zhu, H., et al., *Screening in crystalline liquids protects energetic carriers in hybrid perovskites.* Science, 2016. **353**(6306): p. 1409.

93. Gauthron, K., et al., *Optical spectroscopy of two-dimensional layered (C6H5C2H4-NH3)2-PbI4 perovskite.* Optics Express, 2010. **18**(6): p. 5912-5919.

94. Wu, X., M.T. Trinh, and X.Y. Zhu, *Excitonic Many-Body Interactions in Two-Dimensional Lead Iodide Perovskite Quantum Wells.* The Journal of Physical Chemistry C, 2015. **119**(26): p. 14714-14721.

95. Wang, F., et al., *Solvated Electrons in Solids—Ferroelectric Large Polarons in Lead Halide Perovskites.* Journal of the American Chemical Society, 2020.

96. Smith, M.D., B.A. Connor, and H.I. Karunadasa, *Tuning the luminescence of layered halide perovskites.* Chemical Reviews, 2019. **119**(5): p. 3104-3139.

97. Chong, W.K., D. Giovanni, and T.-C. Sum, *Excitonics in 2D perovskites*, in *Halide Perovskites: Photovoltaics, Light Emitting Devices, and Beyond*. 2018, Wiley-VCH Verlag GmbH & Co. KGaA. p. 55-79.

98. Thirumal, K., et al., *Morphology-independent stable white-light emission from self-assembled two-dimensional perovskites driven by strong exciton-phonon coupling to the oganic famework.* Chemistry of Materials, 2017. **29**(9): p. 3947-3953.

99. Dohner, E.R., et al., *Intrinsic white-light emission from layered hybrid perovskites.* Journal of the American Chemical Society, 2014. **136**(38): p. 13154-13157.

100. Guo, Z., et al., *Electron–Phonon Scattering in Atomically Thin 2D Perovskites.* ACS Nano, 2016. **10**(11): p. 9992-9998.

101. Neutzner, S., et al., *Exciton-polaron spectral structures in two-dimensional hybrid lead-halide perovskites.* Physical Review Materials, 2018. **2**(6): p. 064605.

102. Thouin, F., et al., *Phonon coherences reveal the polaronic character of excitons in two-dimensional lead halide perovskites.* Nature Materials, 2019. **18**(4): p. 349-356.

103. Thouin, F., et al., *Electron-phonon couplings inherent in polarons drive exciton dynamics in two-dimensional metal-halide perovskites.* Chemistry of Materials, 2019. **31**(17): p. 7085-7091.

104. Sum, T.C., M. Righetto, and S.S. Lim, *Quo vadis, perovskite emitters?* The Journal of Chemical Physics, 2020. **152**(13): p. 130901.

105. Milot, R.L., et al., *Charge-carrier dynamics in 2D hybrid metal–halide perovskites.* Nano Letters, 2016. **16**(11): p. 7001-7007.

106. Cho, J., J.T. DuBose, and P.V. Kamat, *Charge carrier recombination dynamics of two-dimensional lead halide perovskites.* The Journal of Physical Chemistry Letters, 2020. **11**(7): p. 2570-2576.

107. Motti, S.G., et al., *Heterogeneous photon recycling and charge diffusion enhance charge transport in quasi-2D lead-halide perovskite films.* Nano Letters, 2019. **19**(6): p. 3953-3960.

108. Shi, E., et al., *Extrinsic and dynamic edge states of two-dimensional lead halide perovskites.* ACS Nano, 2019. **13**(2): p. 1635-1644.

109. Gan, Z., et al., *Transient energy reservoir in 2D perovskites.* Advanced Optical Materials, 2019. **7**(22): p. 1900971.

110. Gan, Z., et al., *The dominant energy transport pathway in halide perovskites: photon recycling or carrier diffusion?* Advanced Energy Materials, 2019. **9**(20): p. 1900185.

111. Quan, L.N., et al., *Tailoring the energy landscape in quasi-2D halide perovskites enables efficient green-light emission.* Nano Letters, 2017. **17**(6): p. 3701-3709.

112. Yuan, M., et al., *Perovskite energy funnels for efficient light-emitting diodes.* Nature Nanotechnology, 2016. **11**(10): p. 872-877.

113. Wang, N., et al., *Perovskite light-emitting diodes based on solution-processed self-organized multiple quantum wells.* Nature Photonics, 2016. **10**(11): p. 699-704.

114. Yantara, N., et al., *Designing the perovskite structural landscape for efficient blue emission.* ACS Energy Letters, 2020: p. 1593-1600.

115. Kulkarni, S.A., et al., *Carrier cascade: enabling high performance perovskite light-emitting diodes (PeLEDs).* Current Opinion in Electrochemistry, 2018. **11**: p. 91-97.

116. Lakowicz, J.R., *Energy transfer*, in *Principles of Fluorescence Spectroscopy*, J.R. Lakowicz, Editor. 1999, Springer US: Boston, MA. p. 367-394.

117. Zhang, L., X. Zhang, and G. Lu, *Band alignment in two-dimensional halide perovskite heterostructures: type I or type II?* The Journal of Physical Chemistry Letters, 2020. **11**(8): p. 2910-2916.

118. Quintero-Bermudez, R., et al., *Ligand-induced surface charge density modulation generates local type-II band alignment in reduced-dimensional perovskites.* Journal of the American Chemical Society, 2019. **141**(34): p. 13459-13467.

119. Proppe, A.H., et al., *Spectrally resolved ultrafast exciton transfer in mixed perovskite quantum wells.* The Journal of Physical Chemistry Letters, 2019. **10**(3): p. 419-426.

120. Wang, J., et al., *Engineered directional charge flow in mixed two-dimensional perovskites enabled by facile cation-exchange.* The Journal of Physical Chemistry C, 2017. **121**(39): p. 21281-21289.

121. Zheng, K., et al., *Inter-phase charge and energy transfer in Ruddlesden–Popper 2D perovskites: critical role of the spacing cations.* Journal of Materials Chemistry A, 2018. **6**(15): p. 6244-6250.

122. Hernández-Martínez, P.L., A.O. Govorov, and H.V. Demir, *Generalized theory of Förster-type nonradiative energy transfer in nanostructures with mixed dimensionality.* The Journal of Physical Chemistry C, 2013. **117**(19): p. 10203-10212.

123. Zhu, H., et al., *Charge transfer dynamics from photoexcited semiconductor quantum dots.* Annual Review of Physical Chemistry, 2016. **67**(1): p. 259-281.

124. Privitera, A., et al., *The central role of ligands in electron transfer from perovskite nanocrystals.* MRS Advances, 2017. **2**(43): p. 2327-2335.

125. Righetto, M., et al., *Engineering interactions in QDs–PCBM blends: a surface chemistry approach.* Nanoscale, 2018. **10**(25): p. 11913-11922.

126. Privitera, A., et al., *Hybrid Organic/Inorganic Perovskite–Polymer Nanocomposites: Toward the Enhancement of Structural and Electrical Properties.* The Journal of Physical Chemistry Letters, 2017. **8**(24): p. 5981-5986.

127. Weidman, M.C., K.G. Yager, and W.A. Tisdale, *Interparticle Spacing and Structural Ordering in Superlattice PbS Nanocrystal Solids Undergoing Ligand Exchange.* Chemistry of Materials, 2015. **27**(2): p. 474-482.

128. Proppe, A.H., et al., *Synthetic control over quantum well width distribution and carrier migration in low-dimensional perovskite photovoltaics.* Journal of the American Chemical Society, 2018. **140**(8): p. 2890-2896.

129. Jin, C., et al., *Ultrafast dynamics in van der Waals heterostructures.* Nature Nanotechnology, 2018. **13**(11): p. 994-1003.

130. Cassette, E., et al., *Room-temperature exciton coherence and dephasing in two-dimensional nanostructures.* Nature Communications, 2015. **6**(1): p. 6086.

131. Cassette, E., et al., *Ultrafast exciton dynamics in 2D in-plane hetero-nanostructures: delocalization and charge transfer.* Physical Chemistry Chemical Physics, 2017. **19**(12): p. 8373-8379.

132. Righetto, M., et al., *Deciphering hot- and multi-exciton dynamics in core–shell QDs by 2D electronic spectroscopies.* Physical Chemistry Chemical Physics, 2018. **20**(27): p. 18176-18183.

133. Beljonne, D., et al., *Beyond Förster resonance energy transfer in biological and nanoscale systems.* The Journal of Physical Chemistry B, 2009. **113**(19): p. 6583-6599.

134. Brédas, J.-L., E.H. Sargent, and G.D. Scholes, *Photovoltaic concepts inspired by coherence effects in photosynthetic systems.* Nature Materials, 2017. **16**(1): p. 35-44.

135. Seiler, H., et al., *Two-dimensional electronic spectroscopy reveals liquid-like lineshape dynamics in CsPbI3 perovskite nanocrystals.* Nature Communications, 2019. **10**(1): p. 4962.

136. Pal, S., et al., *Atomistic analysis of room temperature quantum coherence in two-dimensional CdSe nanostructures.* Nano Letters, 2017. **17**(4): p. 2389-2396.

137. Zhang, Z., et al., *Rapid decoherence suppresses charge recombination in multi-layer 2D halide perovskites: time-domain ab initio analysis.* Nano Letters, 2018. **18**(4): p. 2459-2466.

138. Shang, Q., et al., *Unveiling structurally engineered carrier dynamics in hybrid quasi-two-dimensional perovskite thin films toward controllable emission.* The Journal of Physical Chemistry Letters, 2017. **8**(18): p. 4431-4438.

139. Williams, O.F., et al., *Energy transfer mechanisms in layered 2D perovskites.* The Journal of Chemical Physics, 2018. **148**(13): p. 134706.

140. He, Z., et al., *High-efficiency red light-emitting diodes based on multiple quantum wells of phenylbutylammonium-cesium lead iodide perovskites.* ACS Photonics, 2019. **6**(3): p. 587-594.

141. Sichert, J.A., et al., *Quantum size effect in organometal halide perovskite nanoplatelets.* Nano Letters, 2015. **15**(10): p. 6521-6527.

142. Sichert, J.A., et al., *Tuning the optical bandgap in layered hybrid perovskites through variation of alkyl chain length.* APL Materials, 2019. **7**(4): p. 041116.

143. Zhai, Y., et al., *Giant Rashba splitting in 2D organic-inorganic halide perovskites measured by transient spectroscopies.* Science Advances, 2017. **3**(7): p. e1700704.

144. Giovanni, D., et al., *The Physics of Interlayer Exciton Delocalization in Ruddlesden–Popper Lead Halide Perovskites.* Nano Letters, 2021. **21**(1): p. 405-413.

145. Kim, M., et al., *Switchable S = 1/2 and J = 1/2 Rashba bands in ferroelectric halide perovskites.* Proceedings of the National Academy of Sciences, 2014. **111**(19): p. 6900-6904.

146. Kepenekian, M., et al., *Rashba and Dresselhaus effects in hybrid organic-inorganic perovskites: from basics to devices.* ACS Nano, 2015.

147. Giovanni, D., et al., *Highly spin-polarized carrier dynamics and ultralarge photoinduced magnetization in* $CH_3NH_3PbI_3$ *perovskite thin films.* Nano Letters, 2015. **15**(3): p. 1553-1558.

148. Chen, X., et al., *Impact of layer thickness on the charge carrier and spin coherence lifetime in two-dimensional layered perovskite single crystals.* ACS Energy Letters, 2018. **3**(9): p. 2273-2279.

149. Wang, J., et al., *Spin-optoelectronic devices based on hybrid organic-inorganic trihalide perovskites.* Nature Communications, 2019. **10**(1): p. 129.

150. Zhang, C., et al., *Magnetic field effects in hybrid perovskite devices.* Nature Physics, 2015. **11**: p. 427.

151. Kenichiro, T., et al., *Electronic and excitonic Structures of inorganic-organic perovskite-type quantum-well crystal* $(C_4H_9NH_3)_2PbBr_4$*.* Japanese Journal of Applied Physics, 2005. **44**(8R): p. 5923.

152. Žutić, I., J. Fabian, and S. Das Sarma, *Spintronics: fundamentals and applications.* Review of Modern Physics, 2004. **76**(2): p. 323-410.

153. Odenthal, P., et al., *Spin-polarized exciton quantum beating in hybrid organic-inorganic perovskites.* Nature Physics, 2017. **13**: p. 894–899.

154. Belykh, V.V., et al., *Coherent spin dynamics of electrons and holes in* $CsPbBr_3$ *perovskite crystals.* Nature Communications, 2019. **10**(1): p. 673.

155. Giovanni, D., et al., *Tunable room-temperature spin-selective optical Stark effect in solution-processed layered halide perovskites.* Science Advances, 2016. **2**(6): p. 1600477.

156. Yang, Y., et al., *Large polarization-dependent exciton optical Stark effect in lead iodide perovskites.* Nature Communications, 2016. **7**(1): p. 12613.

157. Todd, S.B., et al., *Detection of Rashba spin splitting in 2D organic-inorganic perovskite via precessional carrier spin relaxation.* APL Materials, 2019. **7**(8): p. 081116.

158. Yang, Y., et al., *Unexpected outstanding room temperature spin transport verified in organic–inorganic hybrid perovskite film.* The Journal of Physical Chemistry Letters, 2019. **10**(15): p. 4422-4428.

159. Wang, K., et al., *Spin-polarized electronic transport through ferromagnet/organic–inorganic hybrid perovskite spinterfaces at room temperature.* Advanced Materials Interfaces, 2019. **6**(19): p. 1900718.

160. Ghosh, D., et al., *Putting the qqueeze on lead iodide perovskites: pressure-induced effects to tune their structural and optoelectronic behavior.* Chemistry of Materials, 2019. **31**(11): p. 4063-4071.

161. Lu, H., et al., *Spin-dependent charge transport through 2D chiral hybrid lead-iodide perovskites.* Science Advances, 2019. **5**(12): p. eaay0571.

162. Long, G., et al., *Spin control in reduced-dimensional chiral perovskites.* Nature Photonics, 2018. **12**(9): p. 528-533.

163. Mitzi, D.B., K. Chondroudis, and C.R. Kagan, *Design, Structure, and Optical Properties of Organic−Inorganic Perovskites Containing an Oligothiophene Chromophore.* Inorganic Chemistry, 1999. **38**(26): p. 6246-6256.

164. Zhu, X.-H., et al., *Effect of Mono- versus Di-ammonium Cation of 2,2‘-Bithiophene Derivatives on the Structure of Organic−Inorganic Hybrid Materials Based on Iodo Metallates.* Inorganic Chemistry, 2003. **42**(17): p. 5330-5339.

165. Ortiz-Cervantes, C., et al., *Thousand-fold Conductivity Increase in 2D Perovskites by Polydiacetylene Incorporation and Doping.* Angewandte Chemie International Edition, 2018. **57**(42): p. 13882-13886.

166. Passarelli, J.V., et al., *Enhanced Out-of-Plane Conductivity and Photovoltaic Performance in n = 1 Layered Perovskites through Organic Cation Design.* Journal of the American Chemical Society, 2018. **140**(23): p. 7313-7323.

167. Gao, Y., et al., *Molecular engineering of organic–inorganic hybrid perovskites quantum wells.* Nature Chemistry, 2019. **11**(12): p. 1151-1157.

168. Gélvez-Rueda, M.C., et al., *Overcoming the exciton binding energy in two-dimensional perovskite nanoplatelets by attachment of conjugated organic chromophores.* Nature Communications, 2020. **11**(1): p. 1901.

169. Liu, C., et al., *Tunable Semiconductors: Control over Carrier States and Excitations in Layered Hybrid Organic-Inorganic Perovskites.* Physical Review Letters, 2018. **121**(14): p. 146401.

170. Dunlap-Shohl, W.A., et al., *Tunable internal quantum well alignment in rationally designed oligomer-based perovskite films deposited by resonant infrared matrix-assisted pulsed laser evaporation.* Materials Horizons, 2019. **6**(8): p. 1707-1716.

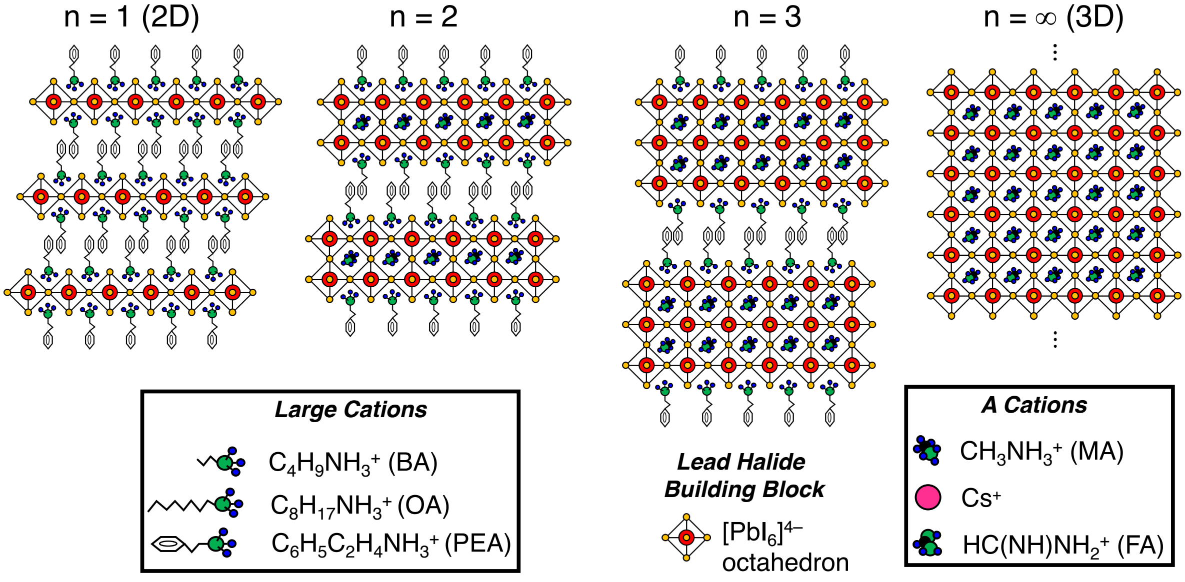
n = 1 (2D)
n = 2
n = 3
n = ∞ (3D)
Large Cations
$C_4H_9NH_3^+$ (BA)
$C_8H_{17}NH_3^+$ (OA)
$C_6H_5C_2H_4NH_3^+$ (PEA)
Lead Halide Building Block
$[PbI_6]^{4-}$ octahedron
A Cations
$CH_3NH_3^+$ (MA)
Cs^+
$HC(NH)NH_2^+$ (FA)

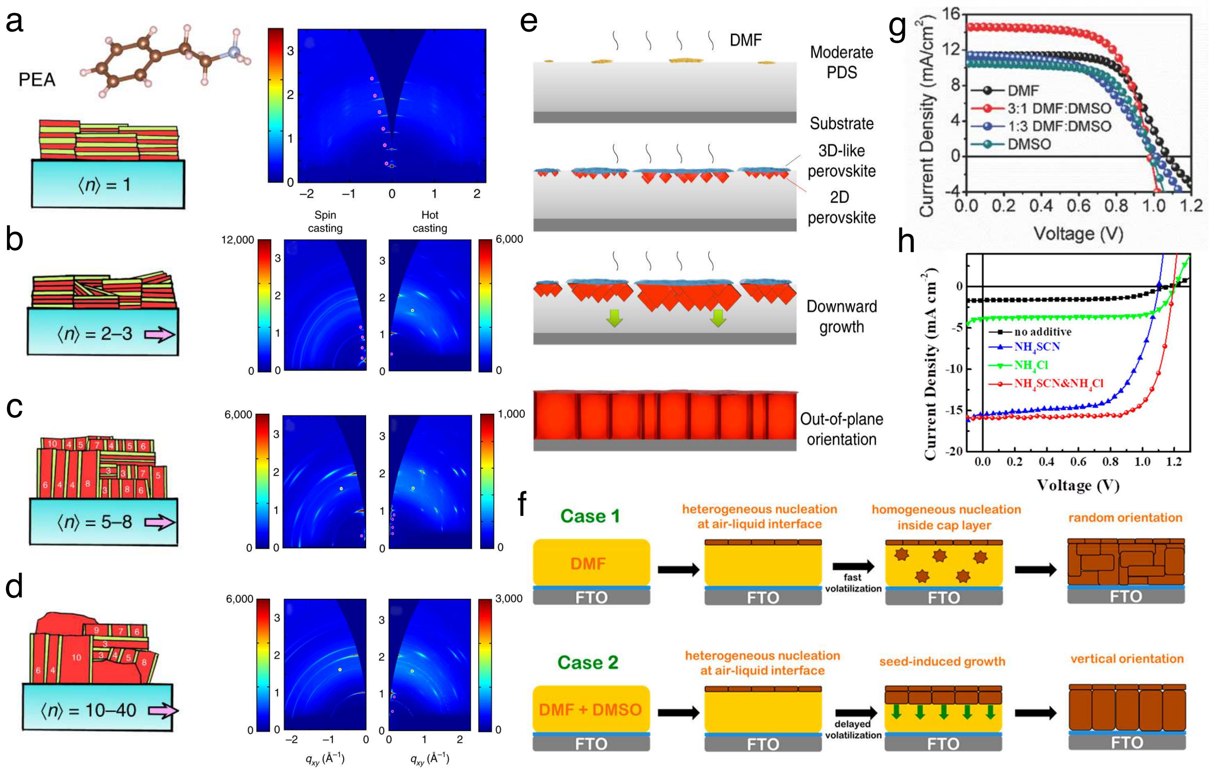
a
PEA
⟨n⟩ = 1
b
⟨n⟩ = 2–3
c
⟨n⟩ = 5–8
d
⟨n⟩ = 10–40
Spin casting
Hot casting
12,000
6,000
1,000
3,000
0
1
2
3
q_{xy} (Å^{-1})
e
DMF
Moderate PDS
Substrate
3D-like perovskite
2D perovskite
Downward growth
Out-of-plane orientation
f
Case 1
DMF
heterogeneous nucleation at air-liquid interface
fast volatilization
homogeneous nucleation inside cap layer
random orientation
Case 2
DMF + DMSO
delayed volatilization
seed-induced growth
vertical orientation
FTO
g
Current Density (mA/cm^2)
Voltage (V)
DMF
3:1 DMF:DMSO
1:3 DMF:DMSO
DMSO
h
Current Density (mA cm^{-2})
Voltage (V)
no additive
NH$_4$SCN
NH$_4$Cl
NH$_4$SCN&NH$_4$Cl

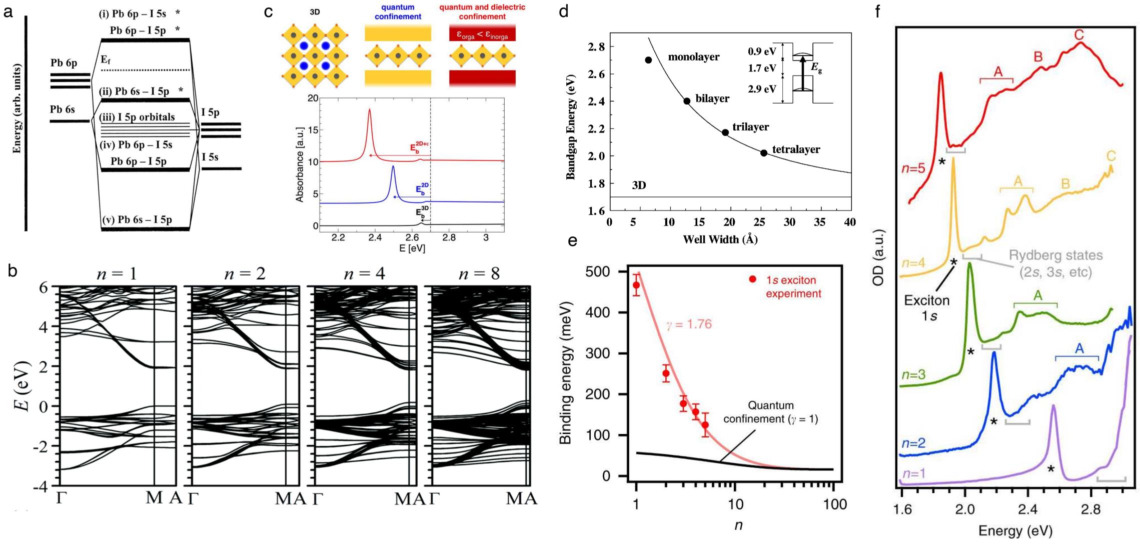
a
Energy (arb. units)
(i) Pb 6p – I 5s *
Pb 6p – I 5p *
Pb 6p
E_f
(ii) Pb 6s – I 5p *
Pb 6s
(iii) I 5p orbitals
I 5p
(iv) Pb 6p – I 5s
Pb 6p – I 5p
I 5s
(v) Pb 6s – I 5p
b
$n = 1$
$n = 2$
$n = 4$
$n = 8$
E (eV)
6
4
2
0
-2
-4
Γ M A Γ M A Γ M A Γ M A
c
3D
quantum confinement
quantum and dielectric confinement
$\varepsilon_{orga} < \varepsilon_{inorga}$
Absorbance [a.u.]
20
15
10
5
0
$E_b^{2D+\varepsilon}$
E_b^{2D}
E_b^{3D}
2.2
2.4
2.6
2.8
3
E [eV]
d
Bandgap Energy (eV)
2.8
2.6
2.4
2.2
2.0
1.8
1.6
monolayer
bilayer
trilayer
tetralayer
3D
0.9 eV
1.7 eV
2.9 eV
E_g
0
5
10
15
20
25
30
35
40
Well Width (Å)
e
Binding energy (meV)
500
400
300
200
100
0
1s exciton experiment
$\gamma = 1.76$
Quantum confinement ($\gamma = 1$)
1
10
100
n
f
OD (a.u.)
A
B
C
n=5
n=4
n=3
n=2
n=1
*
Rydberg states (2s, 3s, etc)
Exciton 1s
1.6
2.0
2.4
2.8
Energy (eV)

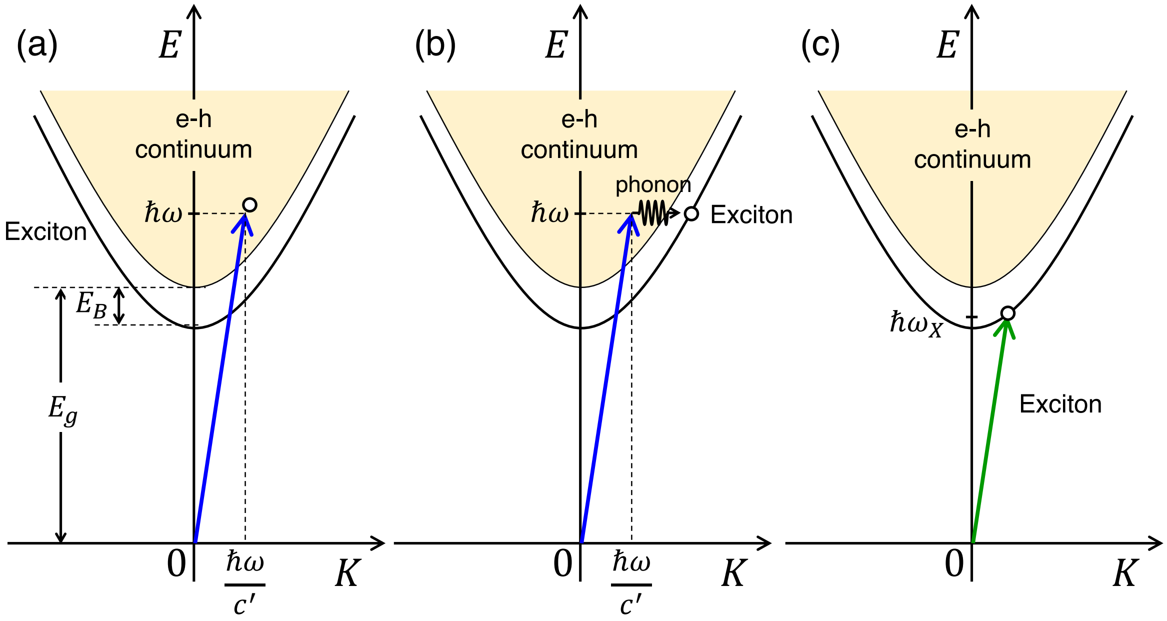
(a)
E
e-h
continuum
ħω
Exciton
E_B
E_g
0
$\frac{\hbar\omega}{c'}$
K
(b)
E
e-h
continuum
phonon
ħω
Exciton
0
$\frac{\hbar\omega}{c'}$
K
(c)
E
e-h
continuum
$\hbar\omega_X$
Exciton
0
K

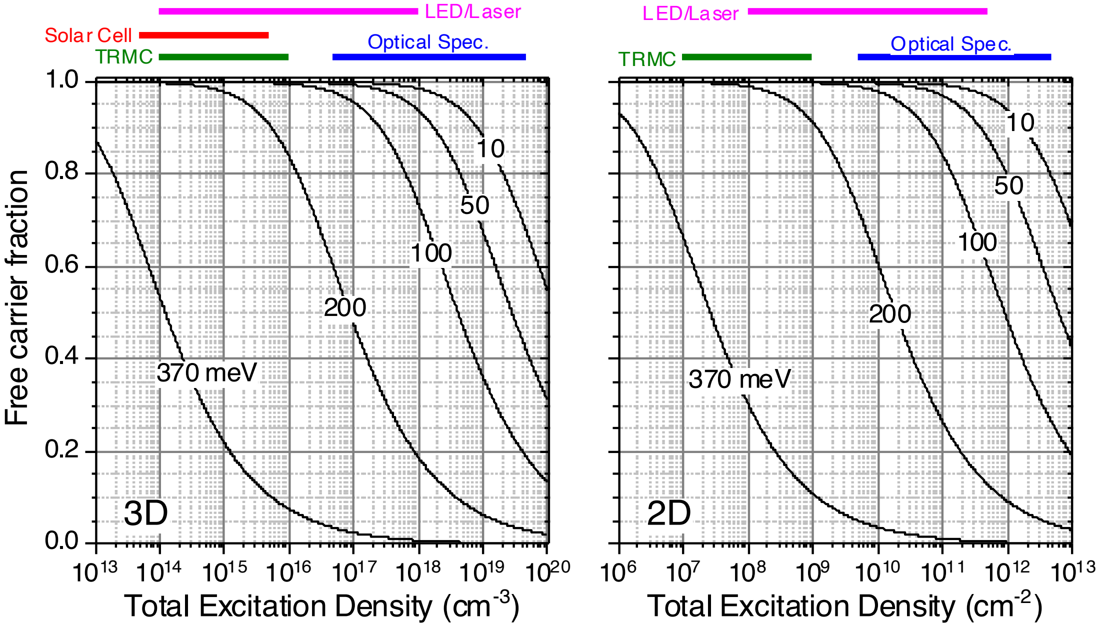
LED/Laser
Solar Cell
TRMC
Optical Spec.
Free carrier fraction
1.0
0.8
0.6
0.4
0.2
0.0
10
50
100
200
370 meV
3D
10^{13}
10^{14}
10^{15}
10^{16}
10^{17}
10^{18}
10^{19}
10^{20}
Total Excitation Density (cm^{-3})
LED/Laser
TRMC
Optical Spec.
10
50
100
200
370 meV
2D
10^{6}
10^{7}
10^{8}
10^{9}
10^{10}
10^{11}
10^{12}
10^{13}
Total Excitation Density (cm^{-2})

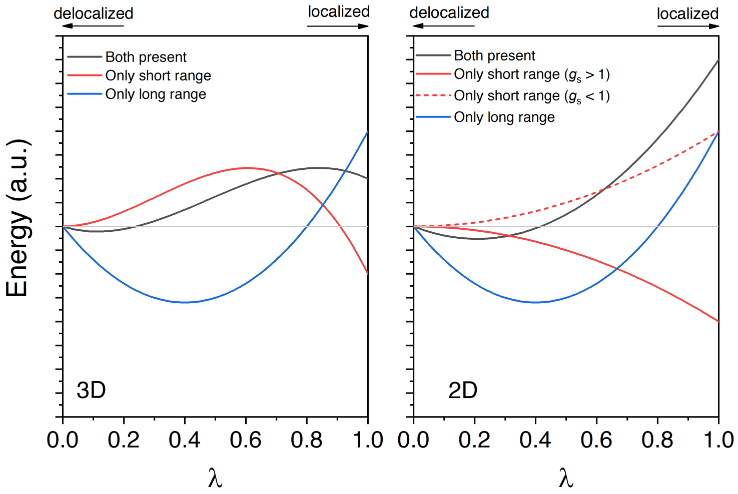
delocalized
localized
Both present
Only short range
Only long range
3D
Energy (a.u.)
0.0
0.2
0.4
0.6
0.8
1.0
λ
delocalized
localized
Both present
Only short range ($g_s > 1$)
Only short range ($g_s < 1$)
Only long range
2D
0.0
0.2
0.4
0.6
0.8
1.0
λ

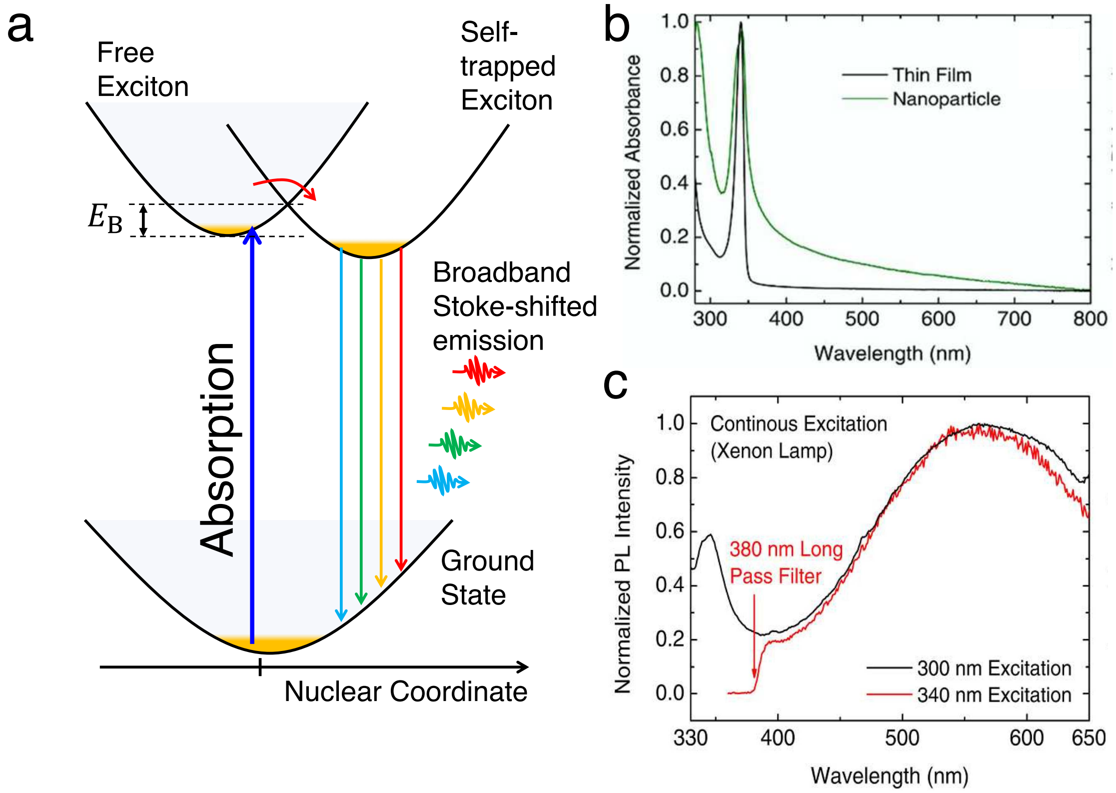
a
Free Exciton
Self-trapped Exciton
E_B
Broadband Stoke-shifted emission
Absorption
Ground State
Nuclear Coordinate
b
Normalized Absorbance
1.0
0.8
0.6
0.4
0.2
0.0
300
400
500
600
700
800
Wavelength (nm)
Thin Film
Nanoparticle
c
Normalized PL Intensity
1.0
0.8
0.6
0.4
0.2
0.0
330
400
500
600
650
Wavelength (nm)
Continous Excitation (Xenon Lamp)
380 nm Long Pass Filter
300 nm Excitation
340 nm Excitation

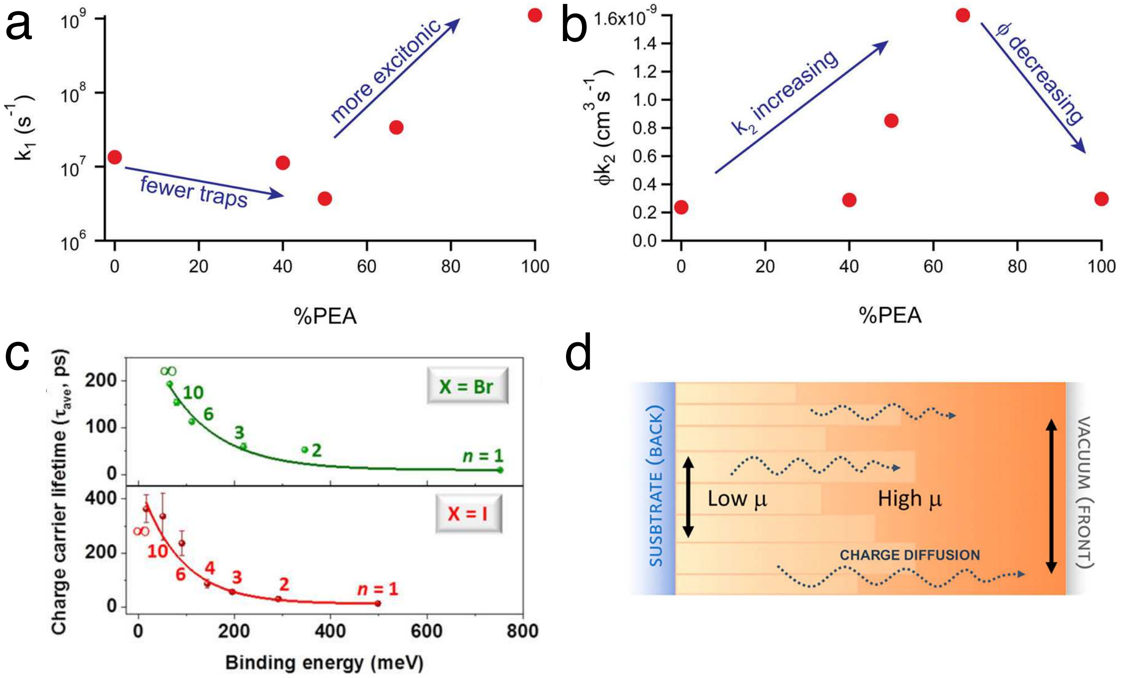
a
10^9
10^8
10^7
10^6
k_1 (s^{-1})
fewer traps
more excitonic
0
20
40
60
80
100
%PEA
b
$1.6x10^{-9}$
1.4
1.2
1.0
0.8
0.6
0.4
0.2
0.0
ϕk_2 ($cm^3 s^{-1}$)
k_2 increasing
ϕ decreasing
0
20
40
60
80
100
%PEA
c
Charge carrier lifetime (τ_{ave}, ps)
200
100
0
X = Br
∞
10
6
3
2
n = 1
400
200
0
X = I
∞
10
6
4
3
2
n = 1
0
200
400
600
800
Binding energy (meV)
d
SUSBTRATE (BACK)
Low μ
High μ
CHARGE DIFFUSION
VACUUM (FRONT)

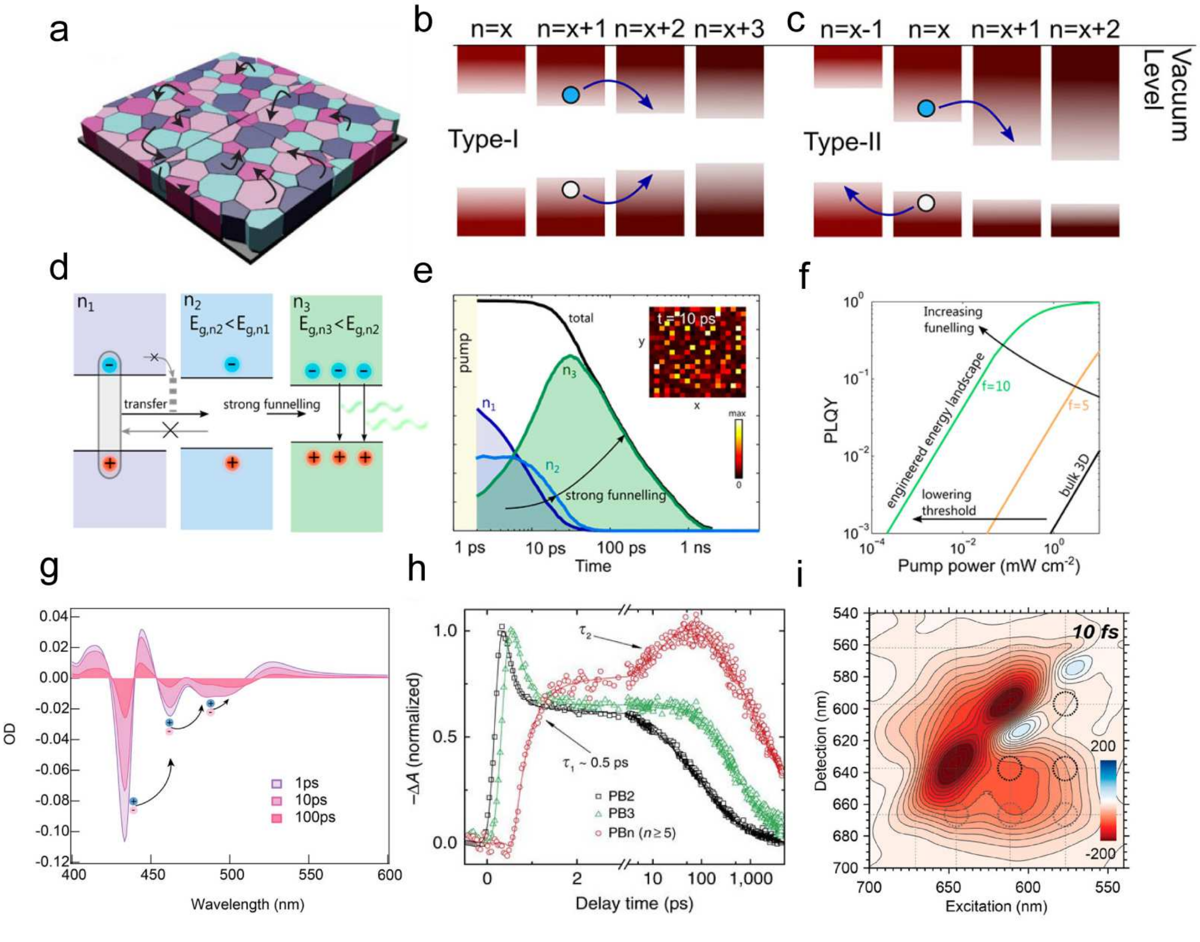
a
b
n=x
n=x+1
n=x+2
n=x+3
Type-I
c
n=x-1
n=x
n=x+1
n=x+2
Vacuum Level
Type-II
d
n_1
n_2
$E_{g,n2}<E_{g,n1}$
n_3
$E_{g,n3}<E_{g,n2}$
transfer
strong funnelling
e
pump
total
t = 10 ps
y
x
max
0
n_1
n_2
n_3
strong funnelling
1 ps
10 ps
100 ps
1 ns
Time
f
10^0
10^{-1}
10^{-2}
10^{-3}
PLQY
Increasing funelling
engineered energy landscape
f=10
f=5
bulk 3D
lowering threshold
10^{-4}
10^{-2}
10^0
Pump power (mW cm^{-2})
g
0.04
0.02
0.00
-0.02
-0.04
-0.06
-0.08
-0.10
-0.12
OD
1ps
10ps
100ps
400
450
500
550
600
Wavelength (nm)
h
1.0
0.5
0.0
$-\Delta A$ (normalized)
τ_2
τ_1 ~ 0.5 ps
PB2
PB3
PBn ($n \geq 5$)
0
2
10
100
1,000
Delay time (ps)
i
10 fs
540
560
580
600
620
640
660
680
700
Detection (nm)
200
-200
700
650
600
550
Excitation (nm)

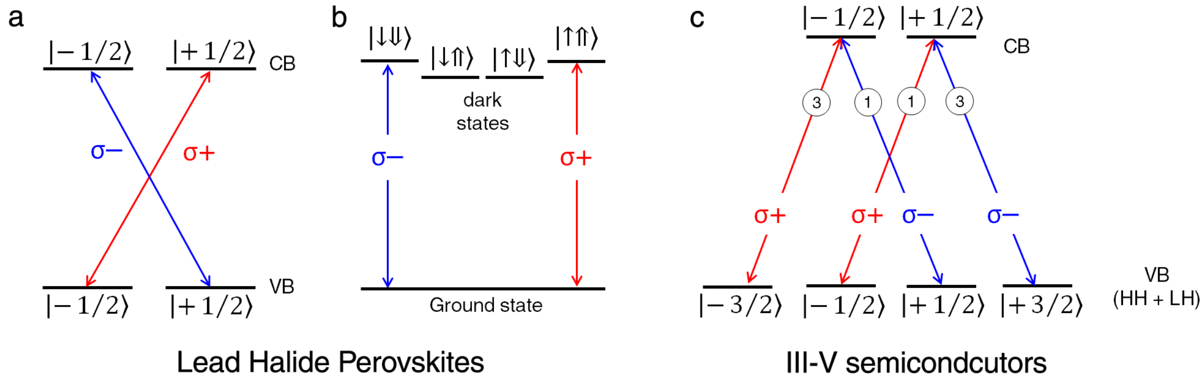
a
|−1/2⟩
|+1/2⟩
CB
σ−
σ+
VB
|−1/2⟩
|+1/2⟩
b
|↓⇓⟩
|↓⇑⟩
|↑⇓⟩
|↑⇑⟩
dark states
σ−
σ+
Ground state
Lead Halide Perovskites
c
|−1/2⟩
|+1/2⟩
CB
③
①
①
③
σ+
σ+
σ−
σ−
|−3/2⟩
|−1/2⟩
|+1/2⟩
|+3/2⟩
VB
(HH + LH)
III-V semicondcutors

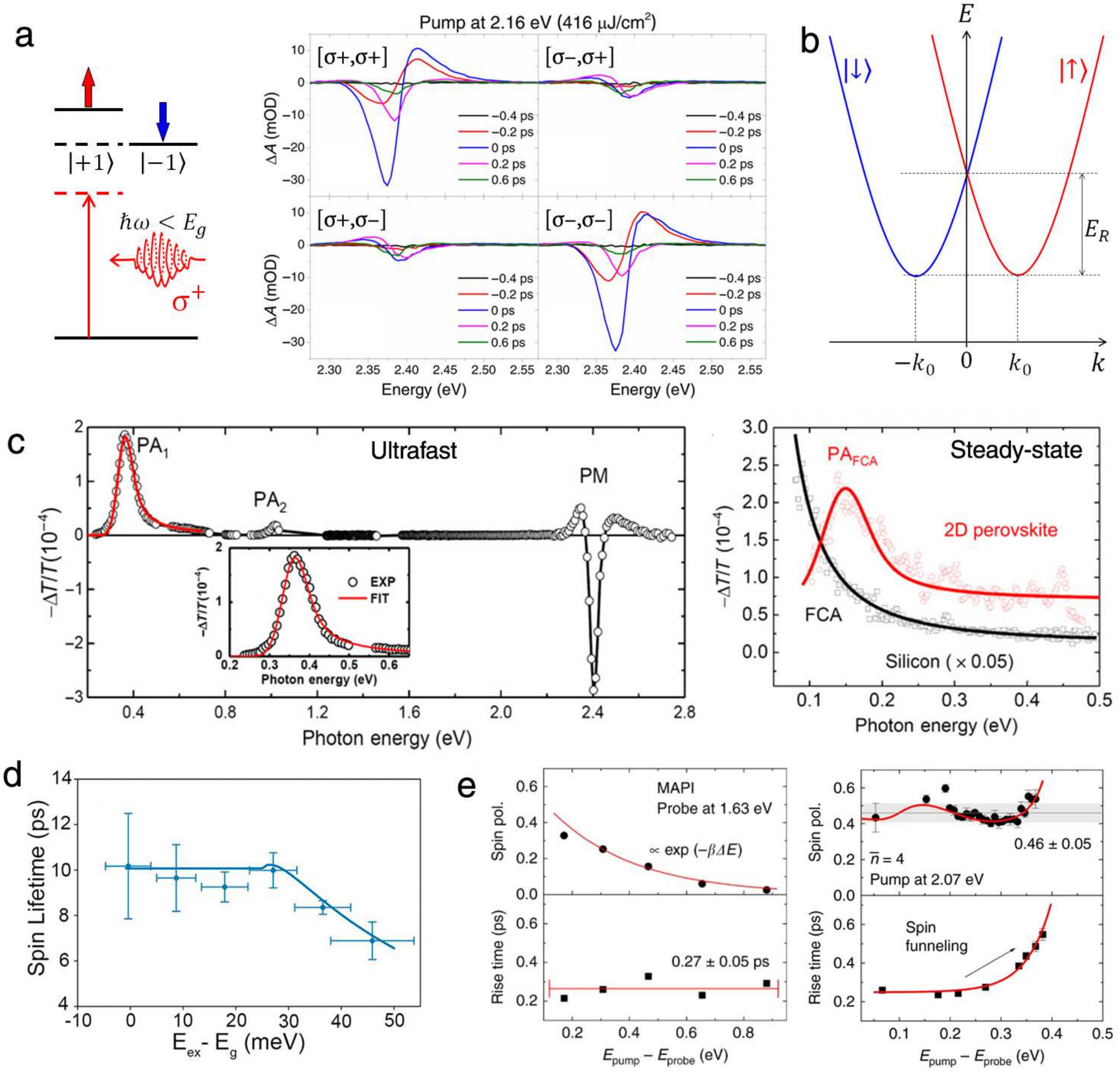
a
|+1⟩
|−1⟩
ℏω < E_g
σ+
Pump at 2.16 eV (416 μJ/cm²)
[σ+,σ+]
[σ−,σ+]
[σ+,σ−]
[σ−,σ−]
ΔA (mOD)
−0.4 ps
−0.2 ps
0 ps
0.2 ps
0.6 ps
Energy (eV)
b
E
|↓⟩
|↑⟩
E_R
−k_0
0
k_0
k
c
Ultrafast
PA1
PA2
PM
−ΔT/T(10⁻⁴)
EXP
FIT
Photon energy (eV)
Steady-state
PA_FCA
2D perovskite
FCA
Silicon (× 0.05)
d
Spin Lifetime (ps)
E_ex - E_g (meV)
e
MAPI
Probe at 1.63 eV
∝ exp (−βΔE)
Spin pol.
Rise time (ps)
0.27 ± 0.05 ps
E_pump − E_probe (eV)
0.46 ± 0.05
n̄ = 4
Pump at 2.07 eV
Spin funneling